Received: 12 November 2018 | Revised: 6 March 2019 | Accepted: 27 March 2019

DOI: 10.1002/nme.6075

RESEARCH ARTICLE

WILEY

Finite rotation exact geometry solid-shell element for laminated composite structures through extended SaS formulation and 3D analytical integration

Gennady M. Kulikov | Svetlana V. Plotnikova

Laboratory of Intelligent Materials and Structures, Tambov State Technical University, Tambov, Russia

Correspondence
Gennady M. Kulikov, Laboratory of Intelligent Materials and Structures, Tambov State Technical University, Sovetskaya Street, 106, Tambov 392000, Russia.
Email: gmkulikov@mail.ru

Funding information
Russian Science Foundation, Grant/Award Number: 18-19-00092; Russian Ministry of Education and Science, Grant/Award Number: 9.4914.2017/6.7

Summary

A nonlinear exact geometry hybrid-mixed four-node solid-shell element using the sampling surfaces (SaS) formulation is developed for the analysis of the second Piola-Kirchhoff stress that extends the authors' finite element (*Int J Numer Methods Eng*. 2019;117:498-522) to laminated composite shells. The SaS formulation is based on choosing inside the layers the arbitrary number of SaS parallel to the middle surface and located at Chebyshev polynomial nodes in order to introduce the displacements of these surfaces as basic shell unknowns. The external surfaces and interfaces are also included into a set of SaS. The proposed hybrid-mixed solid-shell element is based on the Hu-Washizu variational principle and is completely free of shear and membrane locking. The tangent stiffness matrix is evaluated by efficient three-dimensional (3D) analytical integration. As a result, the developed exact geometry solid-shell element exhibits a superior performance in the case of coarse meshes and allows the use of load increments, which are much larger than possible with existing displacement-based solid-shell elements. It could be useful for the 3D stress analysis of thick and thin doubly curved laminated composite shells because the SaS formulation gives the possibility to obtain the 3D solutions with a prescribed accuracy.

KEYWORDS

hybrid-mixed method, laminated composite shell, nonlinear solid-shell element, sampling surfaces method, second Piola-Kirchhoff stress tensor

1 | INTRODUCTION

In recent years, a considerable work has been carried out on finite rotation continuum-based finite elements that can handle the analysis of laminated composite shells satisfactorily. These elements are defined by two layers of nodes at the bottom and top surfaces with three translational degrees of freedom (DOFs) per node and known as six-parameter solid-shell elements.[1-9] However, the six-parameter solid-shell formulation based on the complete constitutive equations is deficient because thickness locking occurs. This is due to the fact that the linear displacement field in the thickness direction results in a constant transverse normal strain, which, in turn, causes artificial stiffening of the shell element in the case of nonvanishing Poisson's ratios. To prevent thickness locking, the three-dimensional (3D) constitutive equations should be modified using the generalized plane stress conditions.[1,2,6,8] The popular enhanced assumed strain (EAS)

method[3,7,9] in which the transverse normal strain is enriched in the thickness direction by a linear term and the hybrid stress method[4,5] in which the transverse normal stress is assumed to be constant through the thickness can be also utilized.

An effective way of using the 3D constitutive equations is to apply the solid-shell element with seven DOFs.[10-20] The seven-parameter shell formulation can be developed choosing six displacements of the bottom and top surfaces and a transverse displacement of the middle surface as basic shell unknowns.[10,18,19] This formulation is optimal with respect to a number of DOF. To overcome locking phenomena, the assumed natural strain (ANS) method,[10-13,15,16] the EAS method[12,14] and the hybrid-mixed method[14,18,19] were used. Applications to laminated composite shells and functionally graded material shells can be found in contributions.[12,17-22]

The more general nine-parameter solid-shell element formulation in which nine displacements of the bottom, middle, and top surfaces are introduced as basic shell unknowns has been developed later.[23,24] Such choice of sampling surfaces (SaS) with the use of Lagrange polynomials of the second degree in through-thickness interpolations of the displacements and strains permits one to present the nonlinear nine-parameter solid-shell element formulation in a very compact form. Moreover, this model makes possible to derive the Green-Lagrange strain tensor, which exactly represents the arbitrarily large rigid-body shell motions in convected curvilinear coordinates. Taking into account that the displacement vectors of SaS are resolved in the middle surface basis, the higher-order shell formulation with nine translational DOFs is suitable to develop the exact geometry or geometrically exact (GeX) solid-shell elements. The term GeX means that the parameterization of the middle surface is known a priori and, therefore, the coefficients of the first and second fundamental forms and Christoffel symbols are taken exactly at element nodes.

The GeX shell elements are attractive due to the fact that, in the geometric modeling of modern CAD systems, the surfaces are usually generated by B-splines or nonuniform rational B-splines (NURBS).[25,26] Accounting for that surfaces are produced by the position vector with representation of two parameters, we can connect the geometric modeling of the shell surface, generated in a CAD system, to the finite element analysis of shell structures. Thus, it is advantageous to use the NURBS surface functions directly in shell calculations and the GeX solid-shell elements are very convenient for this purpose. They also have the two-parameter representation in surfaces and all geometric computations may be done in the middle surface through NURBS surface representations in the CAD system. The NURBS-based isogeometric finite elements and their generalization to T-splines and RHT-splines are very popular because they have some advantages compared to conventional Lagrange-based finite elements. This topic is discussed in many contributions.[27-36]

It is apparent that the GeX shell elements cannot be readily applied to modeling the shells of free-form surfaces. This is because of the fact that the geometric objects such as coefficients of the second fundamental form or curvatures of the middle surface are not easily accessible in a computational context. A methodology of using the CAD systems, particularly bicubic B-spline functions, for the GeX shell elements has been presented by Roh and Cho.[25] However, for describing the surface of revolution, there is no sense to invoke the CAD system technology because, in the literature, there is a simple approach based on the cubic spline functions. This approach has been proposed by Grigolyuk and Kulikov[37] as early as 1982 for describing a shell of revolution whose the middle surface is generated by rotation of the arbitrary curve given on the plane by a discrete number of points with the random errors of measure. To solve a problem, the efficient numerical algorithm of smoothing the data by cubic spline functions[37,38] can be employed. This technique was used later for the analysis of pneumatic tires,[38-42] which are the most widely used composite shell structures of commercial importance today.

It should be noted that the seven- and nine-parameter solid-shell elements do not describe properly the transverse components of the second Piola-Kirchhoff stress tensor in laminated composite shells. To evaluate them without introducing additional DOF, the advanced computational techniques should be adopted; see, eg, papers,[43-45] in which the through-thickness distributions of transverse shear components satisfying the boundary conditions on outer surfaces have been obtained. However, no results for the transverse normal component are documented. The present paper is intended to overcome this shortcoming and develop the higher-order solid-shell elements for calculating all components of the second Piola-Kirchhoff stress tensor in thick and thin shell limits. For this purpose, the GeX nonlinear solid-shell element through the SaS formulation[46,47] is proposed. The SaS laminated shell formulation is based on choosing inside each layer I_n SaS parallel to the middle surface in order to introduce the displacements of these surfaces as fundamental shell unknowns, where $n = 1, 2, \dots, N$; N is the number of layers. Such choice of unknowns with the consequent use of Lagrange polynomials of degree $I_n - 1$ in the through-thickness approximations of displacements, strains, and stresses of the nth layer yields a robust higher-order layerwise shell formulation, in which all basic variables including strains and stresses are related to SaS.

Recently, the SaS formulation has been utilized to develop the four-node flat and curved quadrilateral elements for the linear and nonlinear 3D stress analysis of single-layer homogeneous and functionally graded material plates and shells[48-51] with the SaS located at Chebyshev polynomial nodes. It is important because the SaS formulation with equally spaced SaS[46] does not work properly with the Lagrange polynomials of high degree due to Runge's phenomenon.[47] This phenomenon can yield the oscillation at the edges of the interval when the user deals with some specific functions similar to metric functions involved in the GeX strain-displacement equations. However, the use of Chebyshev polynomial nodes can improve the behavior of the Lagrange polynomials of high degree because such choice permits one to minimize uniformly the error owing to Lagrange interpolation.[47] Therefore, one can calculate the displacements and stresses with a prescribed accuracy employing the sufficient number of SaS.

To circumvent element locking, the hybrid-mixed method pioneered by Pian[52] can be applied efficiently. There are three types of hybrid-mixed shell elements in the literature, namely, the hybrid stress,[4,5,14,53] hybrid strain,[1,2,14,54] and hybrid stress-strain[6,8,18,19,23,24,55] elements. These finite elements are based respectively on the Hellinger-Reissner variational principle[53] with displacements and stresses as independent variables, the modified Hellinger-Reissner variational principle[54] in which the displacements and strains are used as primary variables, and the Hu-Washizu variational principle[55] depending upon displacements, strains, and stresses. The proposed finite rotation GeX/SaS solid-shell element is based on the hybrid stress-strain method and has computational advantages compared to conventional isoparametric hybrid-mixed solid-shell elements.[1,2,4,5,9,14] This is due to the fact that all element matrices require only direct substitutions and no expensive numerical matrix inversion is needed. The advantage of the nonlinear GeX four-node solid-shell element is the use of effective 3D analytical integration[23,24,42,51] that makes possible to utilize the extremely coarse meshes. Besides, the GeX hybrid-mixed solid-shell element allows one to employ the load increments, which are much larger than possible with existing displacement-based solid-shell elements.[3,7,10-17,20] Thus, it can be applied efficiently to large scale computations of doubly curved laminated composite shells undergoing arbitrarily large displacements and rotations.

The proposed finite rotation GeX/SaS solid-shell element formulation is characterized by the following features and new developments.

- We introduce stresses of inner SaS inside the layers and interfaces instead of stress resultants used in previous studies that simplifies the implementation of the hybrid stress-strain method. This novelty allows the presentation of governing equations of the layerwise solid-shell element in terms of only SaS variables.
- The tangent stiffness matrix of the laminated anisotropic sold-shell element is evaluated through efficient 3D analytical integration and its explicit form is given. As a result, the developed GeX/SaS solid-shell element exhibits a superior performance in the case of coarse meshes.

2 | DESCRIPTION OF UNDERFORMED SHELL

Consider a laminated shell of the thickness h. Let the middle surface Ω be described by orthogonal curvilinear coordinates θ_1 and θ_2, which are referred to the lines of principal curvatures of its surface. The coordinate θ_3 is oriented along the unit vector $\mathbf{e}_3(\theta_1, \theta_2)$ normal to the middle surface. Introduce the following notations: $\mathbf{e}_\alpha(\theta_1, \theta_2)$ are the orthonormal base vectors of the middle surface; $\mathbf{r} = \mathbf{r}(\theta_1, \theta_2)$ is the position vector of any point of the middle surface; $\boldsymbol{a}_i(\theta_1, \theta_2)$ are the basis vectors of the middle surface given by

$$\boldsymbol{a}_\alpha = \mathbf{r}_\alpha = A_\alpha \mathbf{e}_\alpha, \quad \boldsymbol{a}_3 = \mathbf{e}_3, \tag{1}$$

where $A_\alpha(\theta_1, \theta_2)$ are the coefficients of the first fundamental form; $\theta_3^{(n)i_n}$ are the coordinates of SaS of the nth layer expressed as

$$\begin{aligned} \theta_3^{(n)1} &= \theta_3^{[n-1]}, \quad \theta_3^{(n)I_n} = \theta_3^{[n]}, \\ \theta_3^{(n)m_n} &= \frac{1}{2}\left(\theta_3^{[n-1]} + \theta_3^{[n]}\right) - \frac{1}{2} h_n \cos\left(\pi \frac{2m_n - 3}{2(I_n - 2)}\right), \end{aligned} \tag{2}$$

where $h_n = \theta_3^{[n]} - \theta_3^{[n-1]}$ is the thickness of the nth layer; $\theta_3^{[m]}$ are the coordinates of interfaces $\Omega^{[m]}$; the index n identifies the belonging of any quantity to the nth layer and runs from 1 to N, whereas the index m identifies the belonging of any quantity to the interface and runs from 1 to $N - 1$; N is the number of layers; the indices m_n running from 2 to $I_n - 1$ describe the inner SaS of the nth layer, whereas the indices i_n, j_n, k_n running from 1 to I_n describe all SaS of the nth layer; I_n is the total number of SaS of the nth layer.

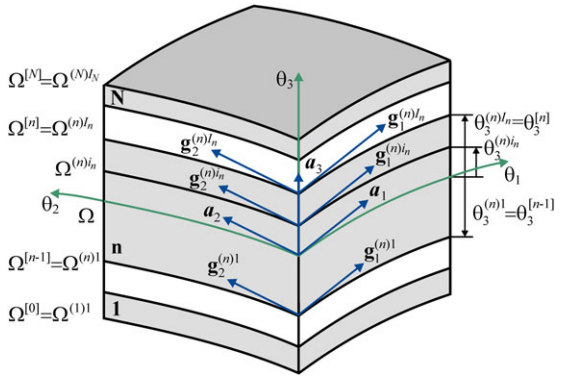

FIGURE 1 Geometry of the laminated shell

Introduce the next group of notations: $\mathbf{R}=\mathbf{r}+\theta_3\mathbf{e}_3$ is the position vector of any point in the shell body; $\mathbf{g}_i$ are the base vectors in the shell body defined as

$$\mathbf{g}_\alpha=\mathbf{R}_{,\alpha}=A_\alpha c_\alpha\mathbf{e}_\alpha,\quad \mathbf{g}_3=\mathbf{R}_{,3}=\mathbf{e}_3, \tag{3}$$

where $c_\alpha=1+k_\alpha\theta_3$ are the components of the shifter tensor; $k_\alpha(\theta_1,\theta_2)$ are the principal curvatures of the middle surface; $\mathbf{R}^{(n)i_n}(\theta_1,\theta_2)=\mathbf{r}+\theta_3^{(n)i_n}\mathbf{e}_3$ are the position vectors of SaS of the nth layer; $\mathbf{g}_i^{(n)i_n}(\theta_1,\theta_2)$ are the base vectors of SaS of the nth layer (see Figure 1) given by

$$\mathbf{g}_\alpha^{(n)i_n}=\mathbf{R}_{,\alpha}^{(n)i_n}=A_\alpha c_\alpha^{(n)i_n}\mathbf{e}_\alpha,\quad \mathbf{g}_3^{(n)i_n}=\mathbf{e}_3, \tag{4}$$

where $c_\alpha^{(n)i_n}(\theta_1,\theta_2)=1+k_\alpha\theta_3^{(n)i_n}$ are components of the shifter tensor on SaS. Here and in the following developments, $(\dots)_{,i}$ stands for the partial derivatives with respect to coordinates θ_i; Greek indices α,β range from 1 to 2; Latin indices i,j,k,l range from 1 to 3.

Remark 1. As can be seen from (2), the transverse coordinates of inner SaS coincide with the coordinates of Chebyshev polynomial nodes (roots of the Chebyshev polynomial of degree I_n-2). This fact has a great meaning for the convergence of the SaS method.[47]

3 | DESCRIPTION OF DEFORMED SHELL

A position vector of the deformed shell is written as

$$\overline{\mathbf{R}}=\mathbf{R}+\mathbf{u}, \tag{5}$$

where $\mathbf{u}$ is the displacement vector, which is always measured in accordance with the total Lagrangian formulation from the initial configuration to the current configuration directly. In particular, the position vectors of SaS of the nth layer are

$$\overline{\mathbf{R}}^{(n)i_n}=\mathbf{R}^{(n)i_n}+\mathbf{u}^{(n)i_n}, \tag{6}$$

$$\mathbf{u}^{(n)i_n}=\mathbf{u}\left(\theta_3^{(n)i_n}\right), \tag{7}$$

where $\mathbf{u}^{(n)i_n}(\theta_1,\theta_2)$ are the displacement vectors of SaS of the nth layer.

The base vectors in the current shell configuration are defined as

$$\overline{\mathbf{g}}_i=\overline{\mathbf{R}}_{,i}=\mathbf{g}_i+\mathbf{u}_{,i}. \tag{8}$$

In particular, the base vectors of deformed SaS of the nth layer (see Figure 2) are

$$\overline{\mathbf{g}}_\alpha^{(n)i_n}=\overline{\mathbf{R}}_{,\alpha}^{(n)i_n}=\mathbf{g}_\alpha^{(n)i_n}+\mathbf{u}_{,\alpha}^{(n)i_n},\quad \overline{\mathbf{g}}_3^{(n)i_n}=\overline{\mathbf{g}}_3\left(\theta_3^{(n)i_n}\right)=\mathbf{e}_3+\boldsymbol{\beta}^{(n)i_n}, \tag{9}$$

$$\boldsymbol{\beta}^{(n)i_n}=\mathbf{u}_{,3}\left(\theta_3^{(n)i_n}\right), \tag{10}$$

where $\boldsymbol{\beta}^{(n)i_n}(\theta_1,\theta_2)$ are the derivative of the displacement vector with respect to coordinate θ_3 at SaS.

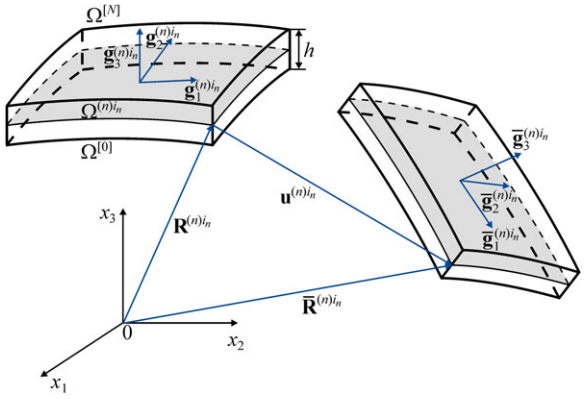

FIGURE 2 Initial and current configurations of the shell [Colour figure can be viewed at wileyonlinelibrary.com]

The Green-Lagrange strain tensor in an orthogonal curvilinear coordinate system can be expressed as

$$2\varepsilon_{ij} = \frac{1}{A_i A_j c_i c_j}\left(\overline{\mathbf{g}}_i \cdot \overline{\mathbf{g}}_j - \mathbf{g}_i \cdot \mathbf{g}_j\right), \tag{11}$$

where $A_3 = 1$ and $c_3 = 1$. In particular, the Green-Lagrange strains of SaS of the nth layer $\varepsilon_{ij}^{(n)i_n}(\theta_1, \theta_2)$ are

$$2\varepsilon_{ij}^{(n)i_n} = 2\varepsilon_{ij}\left(\theta_3^{(n)i_n}\right) = \frac{1}{A_i A_j c_i^{(n)i_n} c_j^{(n)i_n}}\left(\overline{\mathbf{g}}_i^{(n)i_n} \cdot \overline{\mathbf{g}}_j^{(n)i_n} - \mathbf{g}_i^{(n)i_n} \cdot \mathbf{g}_j^{(n)i_n}\right). \tag{12}$$

Substituting base vectors (4) and (9) in strain-displacement equations (12), one obtains

$$\begin{aligned}
2\varepsilon_{\alpha\beta}^{(n)i_n} &= \frac{1}{A_\alpha c_\alpha^{(n)i_n}}\mathbf{u}_{,\alpha}^{(n)i_n} \cdot \mathbf{e}_\beta + \frac{1}{A_\beta c_\beta^{(n)i_n}}\mathbf{u}_{,\beta}^{(n)i_n} \cdot \mathbf{e}_\alpha + \frac{1}{A_\alpha A_\beta c_\alpha^{(n)i_n} c_\beta^{(n)i_n}}\mathbf{u}_{,\alpha}^{(n)i_n} \cdot \mathbf{u}_{,\beta}^{(n)i_n},\\
2\varepsilon_{\alpha 3}^{(n)i_n} &= \frac{1}{A_\alpha c_\alpha^{(n)i_n}}\mathbf{u}_{,\alpha}^{(n)i_n} \cdot \mathbf{e}_3 + \boldsymbol{\beta}^{(n)i_n} \cdot \mathbf{e}_\alpha + \frac{1}{A_\alpha c_\alpha^{(n)i_n}}\mathbf{u}_{,\alpha}^{(n)i_n} \cdot \boldsymbol{\beta}^{(n)i_n},\\
2\varepsilon_{33}^{(n)i_n} &= 2\boldsymbol{\beta}^{(n)i_n} \cdot \mathbf{e}_3 + \boldsymbol{\beta}^{(n)i_n} \cdot \boldsymbol{\beta}^{(n)i_n}.
\end{aligned} \tag{13}$$

Next, we represent the displacement vectors $\mathbf{u}^{(n)i_n}$ and their derivatives $\boldsymbol{\beta}^{(n)i_n}$ in the orthonormal basis $\mathbf{e}_i$ as follows:

$$\mathbf{u}^{(n)i_n} = u_i^{(n)i_n}\mathbf{e}_i, \tag{14}$$

$$\boldsymbol{\beta}^{(n)i_n} = \beta_i^{(n)i_n}\mathbf{e}_i. \tag{15}$$

Here and in the following, the summation on repeated Latin indices is implied.

Using (14) and formulas for the derivatives of unit vectors $\mathbf{e}_i$ with respect to orthogonal curvilinear coordinates,[42] we derive

$$\frac{1}{A_\alpha}\mathbf{u}_{,\alpha}^{(n)i_n} = \lambda_{i\alpha}^{(n)i_n}\mathbf{e}_i, \tag{16}$$

where $\lambda_{i\alpha}^{(n)i_n}$ are the strain parameters of SaS of the nth layer expressed in terms of SaS displacements as

$$\begin{aligned}
&\lambda_{\alpha\alpha}^{(n)i_n} = \frac{1}{A_\alpha}u_{\alpha,\alpha}^{(n)i_n} + B_\alpha u_\beta^{(n)i_n} + k_\alpha u_3^{(n)i_n}, \quad \lambda_{\beta\alpha}^{(n)i_n} = \frac{1}{A_\alpha}u_{\beta,\alpha}^{(n)i_n} - B_\alpha u_\alpha^{(n)i_n} \text{ for } \beta \neq \alpha,\\
&\lambda_{3\alpha}^{(n)i_n} = \frac{1}{A_\alpha}u_{3,\alpha}^{(n)i_n} - k_\alpha u_\alpha^{(n)i_n}, \quad B_\alpha = \frac{1}{A_\alpha A_\beta}A_{\alpha,\beta} \text{ for } \beta \neq \alpha.
\end{aligned} \tag{17}$$

Substitution of Equations (15) and (16) in strain-displacement equations (13) yields

$$\begin{aligned}
2\varepsilon_{\alpha\beta}^{(n)i_n} &= \frac{1}{c_\beta^{(n)i_n}}\lambda_{\alpha\beta}^{(n)i_n} + \frac{1}{c_\alpha^{(n)i_n}}\lambda_{\beta\alpha}^{(n)i_n} + \frac{1}{c_\alpha^{(n)i_n} c_\beta^{(n)i_n}}\lambda_{i\alpha}^{(n)i_n}\lambda_{i\beta}^{(n)i_n},\\
2\varepsilon_{\alpha 3}^{(n)i_n} &= \frac{1}{c_\alpha^{(n)i_n}}\lambda_{3\alpha}^{(n)i_n} + \beta_\alpha^{(n)i_n} + \frac{1}{c_\alpha^{(n)i_n}}\lambda_{i\alpha}^{(n)i_n}\beta_i^{(n)i_n},\\
2\varepsilon_{33}^{(n)i_n} &= 2\beta_3^{(n)i_n} + \beta_i^{(n)i_n}\beta_i^{(n)i_n}.
\end{aligned} \tag{18}$$

Proposition 1. *Three sets of functions $\beta_i^{(n)1}, \beta_i^{(n)2}, \dots, \beta_i^{(n)I_n}$ for each layer are linearly dependent, that is, there exist numbers $\alpha^{(n)1}, \alpha^{(n)2}, \dots, \alpha^{(n)I_n}$, which are not all zero such that*

$$\sum_{i_n} \alpha^{(n)i_n} \beta_i^{(n)i_n} = 0. \tag{19}$$

Proof. This statement is proved using the results.[48] □

4 | THROUGH-THE-THICKNESS DISPLACEMENT AND STRAIN DISTRIBUTIONS

We start now with the first fundamental assumption of the proposed nonlinear higher-order shell theory. Let us assume that the displacements are distributed through the thickness as follows:

$$u_i^{(n)} = \sum_{i_n} L^{(n)i_n} u_i^{(n)i_n}, \quad \theta_3^{[n-1]} \le \theta_3 \le \theta_3^{[n]}, \tag{20}$$

where $L^{(n)i_n}(\theta_3)$ are the Lagrange polynomials of degree $I_n - 1$ defined as

$$L^{(n)i_n} = \prod_{j_n \ne i_n} \frac{\theta_3 - \theta_3^{(n)j_n}}{\theta_3^{(n)i_n} - \theta_3^{(n)j_n}}. \tag{21}$$

The use of Equations (10), (15), and (20) leads to

$$\beta_i^{(n)i_n} = \sum_{j_n} M^{(n)j_n}\left(\theta_3^{(n)i_n}\right) u_i^{(n)j_n}, \tag{22}$$

where $M^{(n)j_n} = L_{,3}^{(n)j_n}$ are the polynomials of degree $I_n - 2$; their values on SaS are

$$\begin{aligned} M^{(n)j_n}\left(\theta_3^{(n)i_n}\right) &= \frac{1}{\theta_3^{(n)j_n} - \theta_3^{(n)i_n}} \prod_{k_n \ne i_n, j_n} \frac{\theta_3^{(n)i_n} - \theta_3^{(n)k_n}}{\theta_3^{(n)j_n} - \theta_3^{(n)k_n}} \text{ for } j_n \ne i_n, \\ M^{(n)i_n}\left(\theta_3^{(n)i_n}\right) &= -\sum_{j_n \ne i_n} M^{(n)j_n}\left(\theta_3^{(n)i_n}\right). \end{aligned} \tag{23}$$

It is seen that the key functions $\beta_i^{(n)i_n}$ of the proposed higher-order shell formulation are represented according to (22) as a linear combination of displacements of SaS $u_i^{(n)j_n}$.

The following step consists in a choice of the consistent approximation of strains through the thickness of the shell. It is apparent that the strain distribution should be chosen similar to displacement distribution (20):

$$\varepsilon_{ij}^{(n)} = \sum_{i_n} L^{(n)i_n} \varepsilon_{ij}^{(n)i_n}, \quad \theta_3^{[n-1]} \le \theta_3 \le \theta_3^{[n]}. \tag{24}$$

Theorem 1. *The Green-Lagrange strain tensor (13) exactly represents large rigid-body motions of SaS in any curvilinear coordinate system.*

Proof. The arbitrarily large rigid-body motion of a shell (see, eg, paper[51]), can be described as

$$(\mathbf{u})^{\text{Rigid}} = \boldsymbol{\Delta} + \boldsymbol{\Phi}\mathbf{R} - \mathbf{R}, \tag{25}$$

where $\Delta = \Delta_i \mathbf{e}_i$ is the constant translation vector; $\boldsymbol{\Phi}$ is the orthogonal rotation matrix. In particular, the rigid-body motions of SaS are written as

$$\left(\mathbf{u}^{(n)i_n}\right)^{\text{Rigid}} = \boldsymbol{\Delta} + \boldsymbol{\Phi}\mathbf{R}^{(n)i_n} - \mathbf{R}^{(n)i_n}. \tag{26}$$

It is apparent that the derivatives of the translation vector and rotation matrix with respect to surface coordinates θ_α are zero, that is,

$$\boldsymbol{\Delta}_{,\alpha} = \mathbf{0}, \quad \boldsymbol{\Phi}_{,\alpha} = \mathbf{0}. \tag{27}$$

Differentiating Equation (26) and taking into account (4) and (27), we obtain

$$\left(\mathbf{u}_{,\alpha}^{(n)i_n}\right)^{\text{Rigid}} = A_\alpha c_\alpha^{(n)i_n}\left(\mathbf{\Phi}\mathbf{e}_\alpha - \mathbf{e}_\alpha\right). \tag{28}$$

Using Equations (15), (22), and (26) and identities

$$\sum_{j_n} M^{(n)j_n}(\theta_3) = 0, \quad \sum_{j_n} \theta_3^{(n)j_n} M^{(n)j_n}(\theta_3) = 1, \tag{29}$$

which, in turn, follow from trivial identities

$$\sum_{j_n} L^{(n)j_n}(\theta_3) = 1, \quad \sum_{j_n} \theta_3^{(n)j_n} L^{(n)j_n}(\theta_3) = \theta_3, \tag{30}$$

one obtains

$$\left(\boldsymbol{\beta}^{(n)i_n}\right)^{\text{Rigid}} = \sum_{j_n} M^{(n)j_n}\left(\theta_3^{(n)i_n}\right)\left(\mathbf{\Phi}\mathbf{R}^{(n)j_n} - \mathbf{R}^{(n)j_n}\right) = \mathbf{\Phi}\mathbf{e}_3 - \mathbf{e}_3. \tag{31}$$

It may be verified utilizing Equations (28) and (31) that strains (13) are zero in a general rigid-body shell motion

$$2\left(\varepsilon_{ij}^{(n)i_n}\right)^{\text{Rigid}} = \mathbf{\Phi}\mathbf{e}_i \cdot \mathbf{\Phi}\mathbf{e}_j - \mathbf{e}_i \cdot \mathbf{e}_j = 0. \tag{32}$$

This conclusion is true because the orthogonal transformation retains the scalar product of vectors. □

Consequence 1. The Green-Lagrange strain tensor (24) exactly represents the large rigid-body motion of a shell in any curvilinear coordinate system.

Proof. The use of Equations (24) and (32) and Theorem 1 leads to

$$\left(\varepsilon_{ij}^{(n)}\right)^{\text{Rigid}} = \sum_{i_n} L^{(n)i_n}\left(\varepsilon_{ij}^{(n)i_n}\right)^{\text{Rigid}} = 0 \tag{33}$$

that completes the proof. □

5 | HU-WASHIZU VARIATIONAL EQUATION FOR LAMINATED SHELL

To develop the geometrically nonlinear hybrid stress-strain solid-shell element formulation, we have to invoke the Hu-Washizu variational principle in which displacements, strains, and stresses are utilized as independent variables

$$\delta J_{\text{HW}} = 0, \tag{34}$$

$$J_{\text{HW}} = \iint\limits_{\Omega} \sum_n \int\limits_{\theta_3^{[n-1]}}^{\theta_3^{[n]}} \left[\frac{1}{2} e_{ij}^{(n)} C_{ijkl}^{(n)} e_{kl}^{(n)} - S_{ij}^{(n)}\left(e_{ij}^{(n)} - \varepsilon_{ij}^{(n)}\right)\right] A_1 A_2 c_1 c_2 d\theta_1 d\theta_2 d\theta_3 - W, \tag{35}$$

$$W = \iint\limits_{\Omega} \left(c_1^+ c_2^+ p_i^+ u_i^{[N]} - c_1^- c_2^- p_i^- u_i^{[0]}\right) A_1 A_2 d\theta_1 d\theta_2 + W_\Sigma, \tag{36}$$

where $S_{ij}^{(n)}$ is the second Piola-Kirchhoff stress tensor of the nth layer; $e_{ij}^{(n)}$ is the displacement-independent strain tensor of the nth layer; $C_{ijkl}^{(n)}$ is the material tensor of the nth layer; $u_i^{[0]}$ and $u_i^{[N]}$ are the displacements of bottom and top surfaces; $c_\alpha^- = 1 - k_\alpha h/2$ and $c_\alpha^+ = 1 + k_\alpha h/2$ are the components of the shifter tensor on outer surfaces; p_i^- and p_i^+ are the tractions on outer surfaces; W_Σ is the work done by external loads applied to the edge surface Σ.

According to the SaS technique, we introduce the through-thickness approximations of stresses and displacement-independent strains choosing them similar to the displacement-dependent strain approximation (24)

$$S_{ij}^{(n)} = \sum_{i_n} L^{(n)i_n} S_{ij}^{(n)i_n}, \quad \theta_3^{[n-1]} \le \theta_3 \le \theta_3^{[n]}, \tag{37}$$

$$e_{ij}^{(n)} = \sum_{i_n} L^{(n)i_n} e_{ij}^{(n)i_n}, \quad \theta_3^{[n-1]} \le \theta_3 \le \theta_3^{[n]}, \tag{38}$$

where $S_{ij}^{(n)i_n} = S_{ij}^{(n)}\left(\theta_3^{(n)i_n}\right)$ is the second Piola-Kirchhoff stress tensor of SaS of the nth layer; $e_{ij}^{(n)i_n} = e_{ij}^{(n)}\left(\theta_3^{(n)i_n}\right)$ is the displacement-independent strain tensor of SaS of the nth layer.

Substituting through-thickness distributions (24), (37), and (38) in Equations (34)-(36) and introducing the weighted coefficients

$$\Lambda^{(n)i_n j_n} = \int_{\theta_3^{[n-1]}}^{\theta_3^{[n]}} L^{(n)i_n} L^{(n)j_n} c_1 c_2 d\theta_3, \tag{39}$$

the following variational equation in terms of SaS variables is obtained:

$$\iint_{\Omega} \sum_{n} \sum_{i_n} \sum_{j_n} \Lambda^{(n)i_n j_n} \Big[\delta\left(\mathbf{e}^{(n)i_n}\right)^{\mathrm{T}} \left(\mathbf{S}^{(n)j_n} - \mathbf{C}^{(n)} \mathbf{e}^{(n)j_n}\right) + \delta\left(\mathbf{S}^{(n)i_n}\right)^{\mathrm{T}} \left(\mathbf{e}^{(n)j_n} - \boldsymbol{\varepsilon}^{(n)j_n}\right) - \delta\left(\boldsymbol{\varepsilon}^{(n)i_n}\right)^{\mathrm{T}} \mathbf{S}^{(n)j_n} \Big] A_1 A_2 d\theta_1 d\theta_2 + \delta W = 0, \tag{40}$$

where

$$\begin{aligned}
\boldsymbol{\varepsilon}^{(n)i_n} &= \left[\varepsilon_{11}^{(n)i_n} \ \varepsilon_{22}^{(n)i_n} \ \varepsilon_{33}^{(n)i_n} \ 2\varepsilon_{12}^{(n)i_n} \ 2\varepsilon_{13}^{(n)i_n} \ 2\varepsilon_{23}^{(n)i_n}\right]^{\mathrm{T}}, \\
\mathbf{e}^{(n)i_n} &= \left[e_{11}^{(n)i_n} \ e_{22}^{(n)i_n} \ e_{33}^{(n)i_n} \ 2e_{12}^{(n)i_n} \ 2e_{13}^{(n)i_n} \ 2e_{23}^{(n)i_n}\right]^{\mathrm{T}}, \\
\mathbf{S}^{(n)i_n} &= \left[S_{11}^{(n)i_n} \ S_{22}^{(n)i_n} \ S_{33}^{(n)i_n} \ S_{12}^{(n)i_n} \ S_{13}^{(n)i_n} \ S_{23}^{(n)i_n}\right]^{\mathrm{T}}, \\
\mathbf{C}^{(n)} &= \begin{bmatrix}
C_{1111}^{(n)} & C_{1122}^{(n)} & C_{1133}^{(n)} & C_{1112}^{(n)} & 0 & 0 \\
C_{2211}^{(n)} & C_{2222}^{(n)} & C_{2233}^{(n)} & C_{2212}^{(n)} & 0 & 0 \\
C_{3311}^{(n)} & C_{3322}^{(n)} & C_{3333}^{(n)} & C_{3312}^{(n)} & 0 & 0 \\
C_{1211}^{(n)} & C_{1222}^{(n)} & C_{1233}^{(n)} & C_{1212}^{(n)} & 0 & 0 \\
0 & 0 & 0 & 0 & C_{1313}^{(n)} & C_{1323}^{(n)} \\
0 & 0 & 0 & 0 & C_{2313}^{(n)} & C_{2323}^{(n)}
\end{bmatrix}.
\end{aligned} \tag{41}$$

6 | GeX FOUR-NODE SOLID-SHELL ELEMENT FORMULATION

The finite element formulation is based on the simple interpolation of the shell via GeX four-node solid-shell elements

$$u_i^{(n)i_n} = \sum_r N_r u_{ir}^{(n)i_n}, \tag{42}$$

$$N_r = \frac{1}{4}\left(1 + n_{1r}\xi_1\right)\left(1 + n_{2r}\xi_2\right), \tag{43}$$

$$n_{1r} = \begin{cases} 1 \text{ for } r = 1,4 \\ -1 \text{ for } r = 2,3 \end{cases}, \quad n_{2r} = \begin{cases} 1 \text{ for } r = 1,2 \\ -1 \text{ for } r = 3,4 \end{cases},$$

where $N_r(\xi_1, \xi_2)$ are the bilinear shape functions of the element; $u_{ir}^{(n)i_n}$ are the displacements of SaS $\Omega^{(n)i_n}$ at element nodes; $\xi_\alpha = (\theta_\alpha - d_\alpha)/\ell_\alpha$ are the normalized curvilinear coordinates (see Figure 3); $2\ell_\alpha$ are the lengths of the element in (θ_1, θ_2)-space; the nodal index r runs from 1 to 4.

To implement the efficient analytical integration throughout the shell element, the extended ANS method[23,42] is utilized to interpolate the displacement-dependent strains

$$\boldsymbol{\varepsilon}^{(n)i_n} = \sum_r N_r \boldsymbol{\varepsilon}_r^{(n)i_n}, \tag{44}$$

$$\boldsymbol{\varepsilon}_r^{(n)i_n} = \left[\varepsilon_{11r}^{(n)i_n} \ \varepsilon_{22r}^{(n)i_n} \ \varepsilon_{33r}^{(n)i_n} \ 2\varepsilon_{12r}^{(n)i_n} \ 2\varepsilon_{13r}^{(n)i_n} \ 2\varepsilon_{23r}^{(n)i_n}\right]^{\mathrm{T}}, \tag{45}$$

where $\varepsilon_{ijr}^{(n)i_n}$ are the strains of SaS of the nth layer at element nodes.

The idea of such approach can be traced back to the ANS method developed by many scientists[3-5,7,9-16] to cure the isoparametric nonlinear solid-shell elements from shear and membrane locking. In contrast to conventional ANS formulations, we treat the term ANS in a broader sense. In the GeX four-node solid-shell element formulation, the displacement-dependent strains of SaS are assumed to vary bilinearly throughout the biunit square in (ξ_1, ξ_2)-space. The extended ANS method (44) makes possible to utilize the element nodes as sampling points that helps to avoid the expensive Gauss numerical integration.

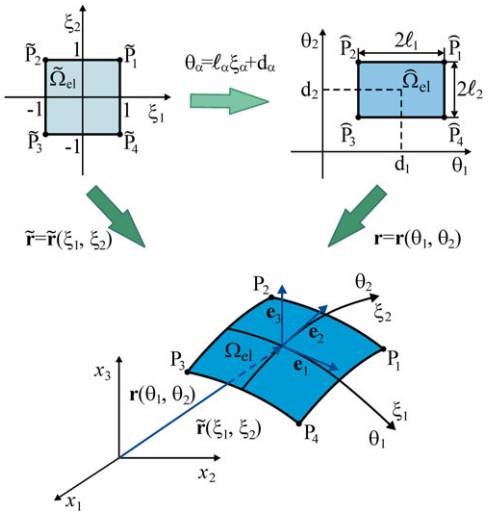

FIGURE 3 Biunit square in (ξ_1, ξ_2)-space mapped into the middle surface of the GeX solid-shell element in (x_1, x_2, x_3)-space

Remark 2. In order to circumvent curvature thickness locking for the finite rotation isoparametric four-node solid-shell element, Betsch and Stein[56] proposed to employ the bilinear interpolation (44) for the transverse normal strain. It is apparent that curvature thickness locking is not related to the GeX four-node solid-shell element because it can handle the arbitrary geometry of surfaces properly. We advocate the use of the extended ANS method (44) for all components of the Green-Lagrange strain tensor to implement the effective analytical integration throughout the element.

Owing to strain-displacement equations (18), the nodal strains of SaS of the nth layer (45) are written as

$$\begin{aligned} 2\varepsilon_{\alpha\beta r}^{(n)i_n} &= \frac{1}{c_{\beta r}^{(n)i_n}}\lambda_{\alpha\beta r}^{(n)i_n} + \frac{1}{c_{\alpha r}^{(n)i_n}}\lambda_{\beta\alpha r}^{(n)i_n} + \frac{1}{c_{\alpha r}^{(n)i_n}c_{\beta r}^{(n)i_n}}\lambda_{i\alpha r}^{(n)i_n}\lambda_{i\beta r}^{(n)i_n}, \\ 2\varepsilon_{\alpha 3r}^{(n)i_n} &= \beta_{\alpha r}^{(n)i_n} + \frac{1}{c_{\alpha r}^{(n)i_n}}\lambda_{3\alpha r}^{(n)i_n} + \frac{1}{c_{\alpha r}^{(n)i_n}}\lambda_{i\alpha r}^{(n)i_n}\beta_{ir}^{(n)i_n}, \quad 2\varepsilon_{33r}^{(n)i_n} = 2\beta_{3r}^{(n)i_n} + \beta_{ir}^{(n)i_n}\beta_{ir}^{(n)i_n}, \end{aligned} \tag{46}$$

where $c_{\alpha r}^{(n)i_n} = 1 + k_{\alpha r}\theta_3^{(n)i_n}$ are the nodal values of the shifter tensor on SaS; $\lambda_{i\alpha r}^{(n)i_n}$ and $\beta_{ir}^{(n)i_n}$ are the strain parameters and displacement derivatives on SaS at element nodes.

Using (17), (22), and (42) and introducing the displacement vector of the shell element

$$\mathbf{q} = \left[\mathbf{q}_1^{\mathrm{T}}\, \mathbf{q}_2^{\mathrm{T}}\, \mathbf{q}_3^{\mathrm{T}}\, \mathbf{q}_4^{\mathrm{T}}\right]^{\mathrm{T}}, \tag{47}$$

$$\mathbf{q}_r = \left[\left(\mathbf{u}_r^{[0]}\right)^{\mathrm{T}}\left(\mathbf{u}_r^{(1)2}\right)^{\mathrm{T}}\cdots\left(\mathbf{u}_r^{(1)I_1-1}\right)^{\mathrm{T}}\left(\mathbf{u}_r^{[1]}\right)^{\mathrm{T}}\left(\mathbf{u}_r^{(2)2}\right)^{\mathrm{T}}\cdots\left(\mathbf{u}_r^{(N-1)I_{N-1}-1}\right)^{\mathrm{T}}\left(\mathbf{u}_r^{[N-1]}\right)^{\mathrm{T}}\left(\mathbf{u}_r^{(N)2}\right)^{\mathrm{T}}\cdots\left(\mathbf{u}_r^{(N)I_N-1}\right)^{\mathrm{T}}\left(\mathbf{u}_r^{[N]}\right)^{\mathrm{T}}\right]^{\mathrm{T}},$$

$$\mathbf{u}_r^{[m]} = \left[\mathbf{u}_{1r}^{[m]}\mathbf{u}_{2r}^{[m]}\mathbf{u}_{3r}^{[m]}\right]^{\mathrm{T}}, \quad \mathbf{u}_r^{(n)m_n} = \left[\mathbf{u}_{1r}^{(n)m_n}\mathbf{u}_{2r}^{(n)m_n}\mathbf{u}_{3r}^{(n)m_n}\right]^{\mathrm{T}},$$

where $u_{ir}^{[0]}$ and $u_{ir}^{[N]}$ are the nodal displacements of bottom and top surfaces; $u_{ir}^{[m]}$ are the nodal displacements of interfaces $\Omega^{[m]}$, one derives

$$\lambda_{i\alpha r}^{(n)i_n} = \left(\boldsymbol{\Xi}_{i\alpha r}^{(n)i_n}\right)^{\mathrm{T}}\mathbf{q}, \quad \beta_{ir}^{(n)i_n} = \left(\boldsymbol{\Xi}_{i3r}^{(n)i_n}\right)^{\mathrm{T}}\mathbf{q}, \tag{48}$$

where $\boldsymbol{\Xi}_{ijr}^{(n)i_n}$ are the *constant* vectors of order $12N_{\mathrm{SaS}}$ (the explicit form of these vectors is given in Appendix A); $N_{\mathrm{SaS}} = \sum_n I_n - N{+}1$ is the total number of SaS.

From Equations (45), (46), and (48) follow

$$\boldsymbol{\varepsilon}_r^{(n)i_n} = \left(\mathbf{B}_r^{(n)i_n} + \mathbf{A}_r^{(n)i_n}(\mathbf{q})\right)\mathbf{q}, \tag{49}$$

where $\mathbf{B}_r^{(n)i_n}$ and $\mathbf{A}_r^{(n)i_n}(\mathbf{q})$ are the nodal matrices of order $6 \times 12N_{\mathrm{SaS}}$ corresponding to linear and nonlinear strain-displacement transformations defined as

$$\mathbf{B}_r^{(n)i_n} = \begin{bmatrix} \left(c_{1r}^{(n)i_n}\right)^{-1}\left(\boldsymbol{\Xi}_{11r}^{(n)i_n}\right)^{\mathrm{T}} \\ \left(c_{2r}^{(n)i_n}\right)^{-1}\left(\boldsymbol{\Xi}_{22r}^{(n)i_n}\right)^{\mathrm{T}} \\ \left(\boldsymbol{\Xi}_{33r}^{(n)i_n}\right)^{\mathrm{T}} \\ \left(c_{2r}^{(n)i_n}\right)^{-1}\left(\boldsymbol{\Xi}_{12r}^{(n)i_n}\right)^{\mathrm{T}} + \left(c_{1r}^{(n)i_n}\right)^{-1}\left(\boldsymbol{\Xi}_{21r}^{(n)i_n}\right)^{\mathrm{T}} \\ \left(\boldsymbol{\Xi}_{13r}^{(n)i_n}\right)^{\mathrm{T}} + \left(c_{1r}^{(n)i_n}\right)^{-1}\left(\boldsymbol{\Xi}_{31r}^{(n)i_n}\right)^{\mathrm{T}} \\ \left(\boldsymbol{\Xi}_{23r}^{(n)i_n}\right)^{\mathrm{T}} + \left(c_{2r}^{(n)i_n}\right)^{-1}\left(\boldsymbol{\Xi}_{32r}^{(n)i_n}\right)^{\mathrm{T}} \end{bmatrix}, \quad \mathbf{A}_r^{(n)i_n}(\mathbf{q}) = \begin{bmatrix} \mathbf{q}^{\mathrm{T}}\boldsymbol{\Pi}_{11r}^{(n)i_n} \\ \mathbf{q}^{\mathrm{T}}\boldsymbol{\Pi}_{22r}^{(n)i_n} \\ \mathbf{q}^{\mathrm{T}}\boldsymbol{\Pi}_{33r}^{(n)i_n} \\ \mathbf{q}^{\mathrm{T}}\boldsymbol{\Pi}_{12r}^{(n)i_n} \\ \mathbf{q}^{\mathrm{T}}\boldsymbol{\Pi}_{13r}^{(n)i_n} \\ \mathbf{q}^{\mathrm{T}}\boldsymbol{\Pi}_{23r}^{(n)i_n} \end{bmatrix}, \tag{50}$$

where $\boldsymbol{\Pi}_{ijr}^{(n)i_n}$ are the *symmetric* matrices of order $12N_{\mathrm{SaS}} \times 12N_{\mathrm{SaS}}$ given by

$$\begin{aligned} \boldsymbol{\Pi}_{ijr}^{(n)i_n} &= \frac{1}{2c_{ir}^{(n)i_n}c_{jr}^{(n)i_n}}\boldsymbol{\Xi}_{kir}^{(n)i_n}\left(\boldsymbol{\Xi}_{kjr}^{(n)i_n}\right)^{\mathrm{T}} \text{ for } i = j, \\ \boldsymbol{\Pi}_{ijr}^{(n)i_n} &= \frac{1}{2c_{ir}^{(n)i_n}c_{jr}^{(n)i_n}}\left[\boldsymbol{\Xi}_{kir}^{(n)i_n}\left(\boldsymbol{\Xi}_{kjr}^{(n)i_n}\right)^{\mathrm{T}} + \boldsymbol{\Xi}_{kjr}^{(n)i_n}\left(\boldsymbol{\Xi}_{kir}^{(n)i_n}\right)^{\mathrm{T}}\right] \text{ for } i < j. \end{aligned} \tag{51}$$

For further developments, it is convenient to rewrite the ANS interpolation (44) as follows:

$$\boldsymbol{\varepsilon}^{(n)i_n} = \sum_{r_1,r_2}(\xi_1)^{r_1}(\xi_2)^{r_2}\boldsymbol{\varepsilon}_{r_1r_2}^{(n)i_n}, \tag{52}$$

$$\boldsymbol{\varepsilon}_{r_1r_2}^{(n)i_n} = \left(\mathbf{B}_{r_1r_2}^{(n)i_n} + \mathbf{A}_{r_1r_2}^{(n)i_n}(\mathbf{q})\right)\mathbf{q}, \tag{53}$$

where

$$\boldsymbol{\varepsilon}_{r_1r_2}^{(n)i_n} = \left[\varepsilon_{11r_1r_2}^{(n)i_n}\ \varepsilon_{22r_1r_2}^{(n)i_n}\ \varepsilon_{33r_1r_2}^{(n)i_n}\ 2\varepsilon_{12r_1r_2}^{(n)i_n}\ 2\varepsilon_{13r_1r_2}^{(n)i_n}\ 2\varepsilon_{23r_1r_2}^{(n)i_n}\right]^{\mathrm{T}}, \tag{54}$$

$$\begin{aligned} \mathbf{B}_{00}^{(n)i_n} &= \frac{1}{4}\left(\mathbf{B}_1^{(n)i_n} + \mathbf{B}_2^{(n)i_n} + \mathbf{B}_3^{(n)i_n} + \mathbf{B}_4^{(n)i_n}\right), \quad \mathbf{B}_{01}^{(n)i_n} = \frac{1}{4}\left(\mathbf{B}_1^{(n)i_n} + \mathbf{B}_2^{(n)i_n} - \mathbf{B}_3^{(n)i_n} - \mathbf{B}_4^{(n)i_n}\right), \\ \mathbf{B}_{10}^{(n)i_n} &= \frac{1}{4}\left(\mathbf{B}_1^{(n)i_n} - \mathbf{B}_2^{(n)i_n} - \mathbf{B}_3^{(n)i_n} + \mathbf{B}_4^{(n)i_n}\right), \quad \mathbf{B}_{11}^{(n)i_n} = \frac{1}{4}\left(\mathbf{B}_1^{(n)i_n} - \mathbf{B}_2^{(n)i_n} + \mathbf{B}_3^{(n)i_n} - \mathbf{B}_4^{(n)i_n}\right), \end{aligned} \tag{55}$$

$$\mathbf{A}_{r_1r_2}^{(n)i_n}(\mathbf{q}) = \begin{bmatrix} \mathbf{q}^{\mathrm{T}}\boldsymbol{\Pi}_{11r_1r_2}^{(n)i_n} \\ \mathbf{q}^{\mathrm{T}}\boldsymbol{\Pi}_{22r_1r_2}^{(n)i_n} \\ \mathbf{q}^{\mathrm{T}}\boldsymbol{\Pi}_{33r_1r_2}^{(n)i_n} \\ \mathbf{q}^{\mathrm{T}}\boldsymbol{\Pi}_{12r_1r_2}^{(n)i_n} \\ \mathbf{q}^{\mathrm{T}}\boldsymbol{\Pi}_{13r_1r_2}^{(n)i_n} \\ \mathbf{q}^{\mathrm{T}}\boldsymbol{\Pi}_{23r_1r_2}^{(n)i_n} \end{bmatrix}, \tag{56}$$

where $\boldsymbol{\Pi}_{ijr_1r_2}^{(n)i_n}$ are the symmetric matrices for $i \le j$ of order $12N_{\mathrm{SaS}} \times 12N_{\mathrm{SaS}}$ defined as

$$\begin{aligned} \boldsymbol{\Pi}_{ij00}^{(n)i_n} &= \frac{1}{4}\left(\boldsymbol{\Pi}_{ij1}^{(n)i_n} + \boldsymbol{\Pi}_{ij2}^{(n)i_n} + \boldsymbol{\Pi}_{ij3}^{(n)i_n} + \boldsymbol{\Pi}_{ij4}^{(n)i_n}\right), \quad \boldsymbol{\Pi}_{ij01}^{(n)i_n} = \frac{1}{4}\left(\boldsymbol{\Pi}_{ij1}^{(n)i_n} + \boldsymbol{\Pi}_{ij2}^{(n)i_n} - \boldsymbol{\Pi}_{ij3}^{(n)i_n} - \boldsymbol{\Pi}_{ij4}^{(n)i_n}\right), \\ \boldsymbol{\Pi}_{ij10}^{(n)i_n} &= \frac{1}{4}\left(\boldsymbol{\Pi}_{ij1}^{(n)i_n} - \boldsymbol{\Pi}_{ij2}^{(n)i_n} - \boldsymbol{\Pi}_{ij3}^{(n)i_n} + \boldsymbol{\Pi}_{ij4}^{(n)i_n}\right), \quad \boldsymbol{\Pi}_{ij11}^{(n)i_n} = \frac{1}{4}\left(\boldsymbol{\Pi}_{ij1}^{(n)i_n} - \boldsymbol{\Pi}_{ij2}^{(n)i_n} + \boldsymbol{\Pi}_{ij3}^{(n)i_n} - \boldsymbol{\Pi}_{ij4}^{(n)i_n}\right). \end{aligned} \tag{57}$$

Here and in the following, the indices r_1 and r_2 run from 0 to 1.

To circumvent shear and membrane locking and have no spurious zero energy modes, the robust stress interpolation[23,51] is utilized

$$\mathbf{S}^{(n)i_n} = \sum_{r_1+r_2<2}(\xi_1)^{r_1}(\xi_2)^{r_2}\mathbf{Q}_{r_1r_2}\mathbf{S}_{r_1r_2}^{(n)i_n}, \tag{58}$$

$$\mathbf{S}_{00}^{(n)i_n} = \left[\varphi_1^{(n)i_n}\ \varphi_2^{(n)i_n}\ \varphi_3^{(n)i_n}\ \varphi_4^{(n)i_n}\ \varphi_5^{(n)i_n}\ \varphi_6^{(n)i_n}\right]^{\mathrm{T}},$$

$$\mathbf{S}_{01}^{(n)i_n} = \left[\varphi_7^{(n)i_n}\ \varphi_9^{(n)i_n}\ \varphi_{11}^{(n)i_n}\right]^{\mathrm{T}}, \quad \mathbf{S}_{10}^{(n)i_n} = \left[\varphi_8^{(n)i_n}\ \varphi_{10}^{(n)i_n}\ \varphi_{12}^{(n)i_n}\right]^{\mathrm{T}},$$

where $\mathbf{Q}_{r_1r_2}$ are the projective matrices given by

$$\mathbf{Q}_{00}=\begin{bmatrix}1&0&0&0&0&0\\0&1&0&0&0&0\\0&0&1&0&0&0\\0&0&0&1&0&0\\0&0&0&0&1&0\\0&0&0&0&0&1\end{bmatrix},\quad \mathbf{Q}_{01}=\begin{bmatrix}1&0&0\\0&0&0\\0&1&0\\0&0&0\\0&0&1\\0&0&0\end{bmatrix},\quad \mathbf{Q}_{10}=\begin{bmatrix}0&0&0\\1&0&0\\0&1&0\\0&0&0\\0&0&0\\0&0&1\end{bmatrix}. \tag{59}$$

The similar interpolation can be used for displacement-independent strains

$$\begin{aligned}\mathbf{e}^{(n)i_n}&=\sum_{r_1+r_2<2}(\xi_1)^{r_1}(\xi_2)^{r_2}\mathbf{Q}_{r_1r_2}\mathbf{e}^{(n)i_n}_{r_1r_2},\\ \mathbf{e}^{(n)i_n}_{00}&=\left[\psi^{(n)i_n}_1\ \psi^{(n)i_n}_2\ \psi^{(n)i_n}_3\ \psi^{(n)i_n}_4\ \psi^{(n)i_n}_5\ \psi^{(n)i_n}_6\right]^{\mathrm{T}},\\ \mathbf{e}^{(n)i_n}_{01}&=\left[\psi^{(n)i_n}_7\ \psi^{(n)i_n}_9\ \psi^{(n)i_n}_{11}\right]^{\mathrm{T}},\quad \mathbf{e}^{(n)i_n}_{10}=\left[\psi^{(n)i_n}_8\ \psi^{(n)i_n}_{10}\ \psi^{(n)i_n}_{12}\right]^{\mathrm{T}}.\end{aligned} \tag{60}$$

Remark 3. Due to interpolation (60), we introduce 12 assumed strain parameters $\psi^{(n)i_n}_1,\psi^{(n)i_n}_2,\dots,\psi^{(n)i_n}_{12}$ for each SaS, ie, $12N_{\mathrm{SaS}}$ for all SaS. It seems to be excessive for the four-node solid-shell element with $12N_{\mathrm{SaS}}$ displacement DOF. However, there exist six dependent strain modes, which provide a correct rank of the element stiffness matrix.[48] This statement can be proved with the help of Proposition 1.

Substituting interpolations (42), (52), (58), and (60) into the Hu-Washizu variational equation (40) and replacing the metric product A_1A_2 in surface integrals by its value at the element center, one can integrate analytically throughout the finite element. As a result, the following equilibrium equations of the GeX hybrid-mixed solid-shell element are obtained:

$$\sum_{j_n}\Lambda^{(n)i_nj_n}\left(\mathbf{S}^{(n)j_n}_{r_1r_2}-\mathbf{Q}^{\mathrm{T}}_{r_1r_2}\mathbf{C}^{(n)}\mathbf{Q}_{r_1r_2}\mathbf{e}^{(n)j_n}_{r_1r_2}\right)=0\ \text{ for }\ r_1+r_2<2, \tag{61}$$

$$\sum_{j_n}\Lambda^{(n)i_nj_n}\left[\mathbf{e}^{(n)j_n}_{r_1r_2}-\mathbf{Q}^{\mathrm{T}}_{r_1r_2}\left(\mathbf{B}^{(n)j_n}_{r_1r_2}+\mathbf{A}^{(n)j_n}_{r_1r_2}(\mathbf{q})\right)\mathbf{q}\right]=0\ \text{ for }\ r_1+r_2<2, \tag{62}$$

$$\sum_{n}\sum_{i_n}\sum_{j_n}\Lambda^{(n)i_nj_n}\sum_{r_1+r_2<2}\frac{1}{3r_1+r_2}\left(\mathbf{B}^{(n)i_n}_{r_1r_2}+2\mathbf{A}^{(n)i_n}_{r_1r_2}(\mathbf{q})\right)^{\mathrm{T}}\mathbf{Q}_{r_1r_2}\mathbf{S}^{(n)j_n}_{r_1r_2}=\mathbf{F}, \tag{63}$$

where $\mathbf{F}$ is the surface traction vector.

Due to the fact that $\det\left(\Lambda^{(n)i_nj_n}\right)\neq 0$ for each layer (see Proposition 2 in Appendix B), the equilibrium equations (61) and (62) can be simplified

$$\mathbf{S}^{(n)i_n}_{r_1r_2}=\mathbf{Q}^{\mathrm{T}}_{r_1r_2}\mathbf{C}^{(n)}\mathbf{Q}_{r_1r_2}\mathbf{e}^{(n)i_n}_{r_1r_2}\ \text{ for }\ r_1+r_2<2, \tag{64}$$

$$\mathbf{e}^{(n)i_n}_{r_1r_2}=\mathbf{Q}^{\mathrm{T}}_{r_1r_2}\left(\mathbf{B}^{(n)i_n}_{r_1r_2}+\mathbf{A}^{(n)i_n}_{r_1r_2}(\mathbf{q})\right)\mathbf{q}\ \text{ for }\ r_1+r_2<2. \tag{65}$$

7 | INCREMENTAL TOTAL LAGRANGIAN FORMULATION

Up to this moment, no incremental arguments are needed in the total Lagrangian formulation. The incremental displacements, strains, and stresses are needed for solving nonlinear equilibrium equations (63)-(65) by a Newton-Raphson method. Further, the left superscripts t and $t+\Delta t$ indicate in which configuration at time t or time $t+\Delta t$ a quantity occurs. In accordance with this agreement, we have

$$\begin{aligned}{}^{t+\Delta t}\mathbf{S}^{(n)i_n}_{r_1r_2}&={}^{t}\mathbf{S}^{(n)i_n}_{r_1r_2}+\Delta\mathbf{S}^{(n)i_n}_{r_1r_2},\quad {}^{t+\Delta t}\mathbf{e}^{(n)i_n}_{r_1r_2}={}^{t}\mathbf{e}^{(n)i_n}_{r_1r_2}+\Delta\mathbf{e}^{(n)i_n}_{r_1r_2},\\ {}^{t+\Delta t}\mathbf{q}&={}^{t}\mathbf{q}+\Delta\mathbf{q},\quad {}^{t+\Delta t}\mathbf{F}={}^{t}\mathbf{F}+\Delta\mathbf{F},\end{aligned} \tag{66}$$

where $\Delta\mathbf{S}^{(n)i_n}_{r_1r_2}$, $\Delta\mathbf{e}^{(n)i_n}_{r_1r_2}$, $\Delta\mathbf{q}$, and $\Delta\mathbf{F}$ are the incremental variables.

Substituting (66) in equilibrium equations (63)-(65) and taking into account that the external loads and the second Piola-Kirchhoff stress constitute the self-equilibrated system in a configuration at time t, one obtains the incremental equations

$$\Delta\mathbf{S}^{(n)i_n}_{r_1r_2}=\mathbf{Q}^{\mathrm{T}}_{r_1r_2}\mathbf{C}^{(n)}\mathbf{Q}_{r_1r_2}\Delta\mathbf{e}^{(n)i_n}_{r_1r_2}\ \text{ for }\ r_1+r_2<2, \tag{67}$$

$$\Delta\mathbf{e}^{(n)i_n}_{r_1r_2}=\mathbf{Q}^{\mathrm{T}}_{r_1r_2}\left({}^{t}\mathbf{M}^{(n)i_n}_{r_1r_2}+\mathbf{A}^{(n)i_n}_{r_1r_2}(\Delta\mathbf{q})\right)\Delta\mathbf{q}\ \text{ for }\ r_1+r_2<2, \tag{68}$$

$$\sum_n \sum_{i_n} \sum_{j_n} \Lambda^{(n)i_n j_n} \sum_{r_1+r_2<2} \frac{1}{3^{r_1+r_2}} \left[2\left(\mathbf{A}_{r_1 r_2}^{(n)i_n}(\Delta\mathbf{q}) \right)^{\mathrm{T}} \mathbf{Q}_{r_1 r_2}\, {}^{t}\mathbf{S}_{r_1 r_2}^{(n)} j_n + \left({}^{t}\mathbf{M}_{r_1 r_2}^{(n)i_n} + 2\mathbf{A}_{r_1 r_2}^{(n)i_n}(\Delta\mathbf{q}) \right)^{\mathrm{T}} \mathbf{Q}_{r_1 r_2} \Delta\mathbf{S}_{r_1 r_2}^{(n)j_n} \right] = \Delta\mathbf{F}, \tag{69}$$

where

$${}^{t}\mathbf{M}_{r_1 r_2}^{(n)i_n} = \mathbf{B}_{r_1 r_2}^{(n)i_n} + 2\mathbf{A}_{r_1 r_2}^{(n)i_n}\left({}^{t}\mathbf{q}\right). \tag{70}$$

Because of incremental equations (68) and (69) are nonlinear, the Newton-Raphson method is employed to linearize them, that is,

$$\begin{gathered} \Delta\mathbf{S}_{r_1 r_2}^{(n)i_n}[k+1] = \Delta\mathbf{S}_{r_1 r_2}^{(n)i_n}[k] + \Delta\widetilde{\mathbf{S}}_{r_1 r_2}^{(n)i_n}[k], \quad \Delta\mathbf{e}_{r_1 r_2}^{(n)i_n}[k+1] = \Delta\mathbf{e}_{r_1 r_2}^{(n)i_n}[k] + \Delta\widetilde{\mathbf{e}}_{r_1 r_2}^{(n)i_n}[k], \\ \Delta\mathbf{q}^{[k+1]} = \Delta\mathbf{q}^{[k]} + \Delta\widetilde{\mathbf{q}}^{[k]}, \quad k = 0, 1, \ldots, \mathrm{NIter}, \end{gathered} \tag{71}$$

where NIter is the number of iterations. By using a standard technique, we arrive at the system of linearized equilibrium equations

$$\Delta\widetilde{\mathbf{S}}_{r_1 r_2}^{(n)i_n}[k] = \mathbf{Q}_{r_1 r_2}^{\mathrm{T}} \mathbf{C}^{(n)} \mathbf{Q}_{r_1 r_2} \Delta\widetilde{\mathbf{e}}_{r_1 r_2}^{(n)i_n}[k] \ \text{ for } \ r_1 + r_2 < 2, \tag{72}$$

$$\begin{aligned} &\Delta\widetilde{\mathbf{e}}_{r_1 r_2}^{(n)i_n}[k] - \mathbf{Q}_{r_1 r_2}^{\mathrm{T}}\, {}^{t}\mathbf{L}_{r_1 r_2}^{(n)i_n}\left(\Delta\mathbf{q}^{[k]}\right)\Delta\widetilde{\mathbf{q}}^{[k]} \\ &= \mathbf{Q}_{r_1 r_2}^{\mathrm{T}}\left({}^{t}\mathbf{L}_{r_1 r_2}^{(n)i_n}\left(\Delta\mathbf{q}^{[k]}\right) - \mathbf{A}_{r_1 r_2}^{(n)i_n}\left(\Delta\mathbf{q}^{[k]}\right)\right)\Delta\mathbf{q}^{[k]} - \Delta\mathbf{e}_{r_1 r_2}^{(n)i_n}[k] \ \text{ for } \ r_1 + r_2 < 2, \end{aligned} \tag{73}$$

$$\begin{aligned} &\sum_n \sum_{i_n} \sum_{j_n} \Lambda^{(n)i_n j_n} \sum_{r_1+r_2<2} \frac{1}{3^{r_1+r_2}} \left[2\left(\mathbf{A}_{r_1 r_2}^{(n)i_n}\left(\Delta\widetilde{\mathbf{q}}^{[k]}\right)\right)^{\mathrm{T}} \mathbf{Q}_{r_1 r_2}\left({}^{t}\mathbf{S}_{r_1 r_2}^{(n)j_n} + \Delta\mathbf{S}_{r_1 r_2}^{(n)j_n}[k]\right) + \left({}^{t}\mathbf{L}_{r_1 r_2}^{(n)i_n}\left(\Delta\mathbf{q}^{[k]}\right)\right)^{\mathrm{T}} \times \mathbf{Q}_{r_1 r_2}\Delta\widetilde{\mathbf{S}}_{r_1 r_2}^{(n)j_n}[k] \right] \\ &= \Delta\mathbf{F} - \sum_n \sum_{i_n} \sum_{j_n} \Lambda^{(n)i_n j_n} \sum_{r_1+r_2<2} \frac{1}{3^{r_1+r_2}} \left[2\left(\mathbf{A}_{r_1 r_2}^{(n)i_n}\left(\Delta\mathbf{q}^{[k]}\right)\right)^{\mathrm{T}} \mathbf{Q}_{r_1 r_2}\, {}^{t}\mathbf{S}_{r_1 r_2}^{(n)j_n} + \left({}^{t}\mathbf{L}_{r_1 r_2}^{(n)i_n}\left(\Delta\mathbf{q}^{[k]}\right)\right)^{\mathrm{T}} \mathbf{Q}_{r_1 r_2}\Delta\mathbf{S}_{r_1 r_2}^{(n)j_n}[k] \right], \end{aligned} \tag{74}$$

where

$${}^{t}\mathbf{L}_{r_1 r_2}^{(n)i_n}\left(\Delta\mathbf{q}^{[k]}\right) = \mathbf{B}_{r_1 r_2}^{(n)i_n} + 2\mathbf{A}_{r_1 r_2}^{(n)i_n}\left({}^{t}\mathbf{q} + \Delta\mathbf{q}^{[k]}\right). \tag{75}$$

Owing to Proposition 3 (see Appendix B), Equation (74) can be written in a more convenient form

$$\begin{aligned} &\sum_n \sum_{i_n} \sum_{j_n} \Lambda^{(n)i_n j_n} \sum_{r_1+r_2<2} \frac{1}{3^{r_1+r_2}} \left[2\mathbf{H}_{r_1 r_2}^{(n)i_n}\left(\mathbf{Q}_{r_1 r_2}\left({}^{t}\mathbf{S}_{r_1 r_2}^{(n)j_n} + \Delta\mathbf{S}_{r_1 r_2}^{(n)j_n}[k]\right)\right)\Delta\widetilde{\mathbf{q}}^{[k]} + \left({}^{t}\mathbf{L}_{r_1 r_2}^{(n)i_n}\left(\Delta\mathbf{q}^{[k]}\right)\right)^{\mathrm{T}} \times \mathbf{Q}_{r_1 r_2}\Delta\widetilde{\mathbf{S}}_{r_1 r_2}^{(n)j_n}[k] \right] \\ &= \Delta\mathbf{F} - \sum_n \sum_{i_n} \sum_{j_n} \Lambda^{(n)i_n j_n} \sum_{r_1+r_2<2} \frac{1}{3^{r_1+r_2}} \left[2\mathbf{H}_{r_1 r_2}^{(n)i_n}\left(\mathbf{Q}_{r_1 r_2}\, {}^{t}\mathbf{S}_{r_1 r_2}^{(n)j_n}\right)\Delta\mathbf{q}^{[k]} + \left({}^{t}\mathbf{L}_{r_1 r_2}^{(n)i_n}\left(\Delta\mathbf{q}^{[k]}\right)\right)^{\mathrm{T}} \mathbf{Q}_{r_1 r_2}\Delta\mathbf{S}_{r_1 r_2}^{(n)j_n}[k] \right]. \end{aligned} \tag{76}$$

Eliminating incremental stresses $\widetilde{\mathbf{S}}_{r_1 r_2}^{(n)i_n}[k]$ and strains $\Delta\widetilde{\mathbf{e}}_{r_1 r_2}^{(n)i_n}[k]$ from Equations (72), (73), and (76), we arrive at the system of linear equations

$$\mathbf{K}_{\mathrm{T}}\Delta\widetilde{\mathbf{q}}^{[k]} = \boldsymbol{\Delta}\mathbf{F}^{[k]}, \tag{77}$$

where $\mathbf{K}_{\mathrm{T}} = \mathbf{K}_{\mathrm{D}} + \mathbf{K}_{\mathrm{H}}$ is the tangent stiffness matrix of order $12N_{\mathrm{SaS}} \times 12N_{\mathrm{SaS}}$; $\boldsymbol{\Delta}\mathbf{F}^{[k]}$ is the right-hand side vector given by

$$\mathbf{K}_{\mathrm{D}} = \sum_n \sum_{i_n} \sum_{j_n} \Lambda^{(n)i_n j_n} \sum_{r_1+r_2<2} \frac{1}{3^{r_1+r_2}} \left({}^{t}\mathbf{L}_{r_1 r_2}^{(n)i_n}\left(\Delta\mathbf{q}^{[k]}\right)\right)^{\mathrm{T}} \mathbf{C}_{r_1 r_2}^{(n)}\, {}^{t}\mathbf{L}_{r_1 r_2}^{(n)j_n}\left(\Delta\mathbf{q}^{[k]}\right), \tag{78}$$

$$\mathbf{K}_{\mathrm{H}} = 2\sum_n \sum_{i_n} \sum_{j_n} \Lambda^{(n)i_n j_n} \sum_{r_1+r_2<2} \frac{1}{3^{r_1+r_2}} \mathbf{H}_{r_1 r_2}^{(n)i_n}\left(\mathbf{Q}_{r_1 r_2}\left({}^{t}\mathbf{S}_{r_1 r_2}^{(n)j_n} + \Delta\mathbf{S}_{r_1 r_2}^{(n)j_n}[k]\right)\right), \tag{79}$$

$$\begin{aligned} \boldsymbol{\Delta}\mathbf{F}^{[k]} = \boldsymbol{\Delta}\mathbf{F} - \sum_n \sum_{i_n} \sum_{j_n} \Lambda^{(n)i_n j_n} \sum_{r_1+r_2<2} \frac{1}{3^{r_1+r_2}} &\left[\left({}^{t}\mathbf{L}_{r_1 r_2}^{(n)i_n}\left(\Delta\mathbf{q}^{[k]}\right)\right)^{\mathrm{T}} \mathbf{C}_{r_1 r_2}^{(n)} \right. \\ &\left. \times \left({}^{t}\mathbf{L}_{r_1 r_2}^{(n)j_n}\left(\Delta\mathbf{q}^{[k]}\right) - \mathbf{A}_{r_1 r_2}^{(n)j_n}\left(\Delta\mathbf{q}^{[k]}\right)\right) + 2\mathbf{H}_{r_1 r_2}^{(n)i_n}\left(\mathbf{Q}_{r_1 r_2}\, {}^{t}\mathbf{S}_{r_1 r_2}^{(n)j_n}\right)\right]\Delta\mathbf{q}^{[k]}, \end{aligned} \tag{80}$$

where

$$\mathbf{C}_{r_1 r_2}^{(n)} = \mathbf{Q}_{r_1 r_2}\mathbf{Q}_{r_1 r_2}^{\mathrm{T}}\mathbf{C}^{(n)}\mathbf{Q}_{r_1 r_2}\mathbf{Q}_{r_1 r_2}^{\mathrm{T}}. \tag{81}$$

For computing the incremental stresses $\Delta\mathbf{S}_{r_1 r_2}^{(n)i_n}[k]$ from Equation (79), we employ the advanced finite element technique based on the use of linearized equations (67) and (68)

$$\Delta\mathbf{S}_{r_1 r_2}^{(n)i_n}[k] = \mathbf{Q}_{r_1 r_2}^{\mathrm{T}}\mathbf{C}^{(n)}\mathbf{Q}_{r_1 r_2}\Delta\mathbf{e}_{r_1 r_2}^{(n)i_n}[k] \ \text{ for } \ r_1 + r_2 < 2, \tag{82}$$

$$\Delta\mathbf{e}_{r_1 r_2}^{(n)i_n}[k] = \mathbf{Q}_{r_1 r_2}^{\mathrm{T}}\left({}^{t}\mathbf{L}_{r_1 r_2}^{(n)i_n}\left(\Delta\mathbf{q}^{[k-1]}\right)\Delta\mathbf{q}^{[k]} - \mathbf{A}_{r_1 r_2}^{(n)i_n}\left(\Delta\mathbf{q}^{[k-1]}\right)\Delta\mathbf{q}^{[k-1]}\right) \ \text{ for } \ r_1 + r_2 < 2. \tag{83}$$

These equations hold for $k \geq 1$ and, at the beginning of each iteration process, one should set

$$\Delta \mathbf{q}^{[0]} = \mathbf{0}, \quad \Delta \mathbf{e}_{r_1 r_2}^{(n) i_n [0]} = \mathbf{0}. \tag{84}$$

The proposed incremental approach allows the use of load increments, which are much larger than possible with GeX displacement-based solid-shell element formulations.[1,8] This is because of the fact that an additional load vector due to compatibility mismatch (82) and (83) at the kth iteration step is present in linearized equilibrium equations (77) and disappears only at the end of the iteration process as discussed in works.[8,57-59]

Remark 4. As expected, the tangent stiffness matrix $\mathbf{K}_{\mathrm{T}}$ is symmetric. This is due to the symmetry of matrices $\mathbf{K}_{\mathrm{D}}$ and $\mathbf{K}_{\mathrm{H}}$. The symmetry of the latter matrix follows directly from the symmetry of matrices $\mathbf{H}_{r_1 r_2}^{(n) i_n}$ (see Proposition 3 in Appendix B).

Remark 5. To calculate the weighted coefficients $\Lambda^{(n) i_n j_n}$ from Equations (78)-(80), we utilize the (I_n+1)-point Gaussian quadrature rule in order to fulfill *exact* integration in (39). This is sufficient because $L^{(n) i_n}$ are the Lagrange basis polynomials of degree $I_n - 1$ and c_α are the first degree polynomials.

Remark 6. It is worth noting that the element matrices (78)-(80) are evaluated with no expensive numerical matrix inversion that is impossible in the framework of the conventional isoparametric hybrid-mixed solid-shell element formulation.[1,2,4,5,9,14] Recalling that the tangent stiffness matrix is computed by using analytical integration throughout the element, the developed nonlinear GeX solid-shell element is very economical and efficient. Moreover, it permits the use of extremely coarse meshes as demonstrated in benchmarks considered in Section 8.

The equilibrium equations (77) for each element are assembled by a standard technique to form the global equilibrium equations. These incremental equations should be performed until the required accuracy of the solution is reached. Herein, two convergence criteria are employed to assess the potential of the proposed GeX four-node solid-shell element

$$\left\| \Delta \mathbf{U}^{[k+1]} - \Delta \mathbf{U}^{[k]} \right\| < \varepsilon \left\| \Delta \mathbf{U}^{[k]} \right\|, \tag{85}$$

$$\left\| \mathbf{r}^{[k]} \right\| < \varepsilon \left\| \mathbf{r}^{[0]} \right\|, \tag{86}$$

where $\| \ldots \|$stands for the Euclidean norm; $\Delta \mathbf{U}$ is the global vector of displacement increments; $\mathbf{r}$ is the residual vector; ε is the prescribed tolerance.

8 | BENCHMARK PROBLEMS

The performance of the developed GeX laminated composite four-node solid-shell element called the GeXSaS4 element is evaluated with nonlinear seven- and nine-parameter solid-shell elements and solid elements extracted from the literature. A listing of the elements and the abbreviations used to identify them are contained in Table 1. The derived results are compared with those based as a rule on using the identical node spacing and the same convergence criterion and tolerance. In this section, NStep denotes a number of load steps employed to *equally* divide the maximum load, whereas NIter stands for a total number of Newton iterations.

TABLE 1 Listing of nonlinear shell elements

Name	Description
GeXSaS4	GeX four-node SaS solid-shell element developed
GeX7P4	GeX seven-parameter four-node solid-shell element[18]
GeX9P4	GeX nine-parameter four-node solid-shell element[23]
GeX7PH	GeX seven-parameter higher-order solid-shell element[17]
ISO7PH	Isoparametric seven-parameter higher-order solid-shell element[20]
Solid45	Isoparametric ANSYS four-node solid element[60]

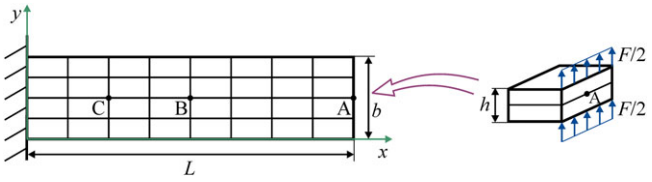

FIGURE 4 Cantilever plate strip subjected to end shear loading [Colour figure can be viewed at wileyonlinelibrary.com]

TABLE 2 Convergence study for the angle-ply plate strips under shear load $F = 5$ using three SaS inside each layer and the displacement-based criterion with $\varepsilon = 10^{-4}$

	[−45/45/−45/45]						[30/−60/−60/30]					
Mesh	**4 × 2**	**8 × 4**	**16 × 4**	**32 × 8**	**64 × 8**	**Solid45[a] 64 × 8**	**4 × 2**	**8 × 4**	**16 × 4**	**32 × 8**	**64 × 8**	**Solid45[a] 64 × 8**
$\overline{u}_3$ (A)	8.373	8.343	8.353	8.363	8.366	8.365	8.067	8.048	8.053	8.061	8.064	8.063
$-\overline{u}_1$ (A)	6.174	6.134	6.145	6.158	6.161	6.158	5.585	5.563	5.568	5.579	5.581	5.579
NStep	1	1	1	1	1	105	1	1	1	1	1	50
NIter	6	6	6	6	6	362	6	6	6	6	6	221

[a]Two elements were used through the layer thickness that corresponds to a chosen number of SaS.

TABLE 3 Euclidean norm of displacement and residual vectors during equilibrium iterations for the [−45/45/−45/45] plate strip for a different number of SaS inside each layer I_n using 32 × 8 mesh when the total load $F = 5$ is applied in one single step

	$\|\| \mathbf{U}^{[n+1]} - \mathbf{U}^{[n]} \|\|$		$\|\| \mathbf{r}^{[n]} \|\|$	
Iteration	$I_n = 3$	$I_n = 4$	$I_n = 3$	$I_n = 4$
0	1.19E+03	1.43E+03	1.21E+00	1.21E+00
1	5.83E+02	7.01E+02	3.75E+07	3.76E+07
2	2.67E+02	3.21E+02	4.70E+06	4.71E+06
3	1.01E+02	1.21E+02	5.88E+05	5.89E+05
4	2.13E+01	2.56E+01	6.71E+04	6.73E+04
5	1.52E+00	1.83E+00	4.37E+03	4.39E+03
6	2.03E−02	2.44E−02	4.19E+01	4.21E+01
7	2.01E−05	2.42E−05	7.47E−03	7.52E−03
8	1.35E−11	6.77E−11	6.13E−09	1.31E−08
9	1.06E−11	6.72E−11	4.58E−09	1.40E−08

8.1 | Cantilever plate strip under end shear loading

This example has been considered by many researchers to test the nonlinear shell elements for thin-walled structures undergoing finite rotations (see, eg, papers[17,20,61]). The strip with geometric parameters $L = 10$, $h = 0.1$, and $b = 1$ is subjected to the end shear load F as shown in Figure 4. We study the laminated composite plate strips with material properties $E_L = 10^6$, $E_T = 0.3 \times 10^6$, $G_{LT} = 0.15 \times 10^6$, $G_{TT} = 0.12 \times 10^6$, and $\nu_{LT} = \nu_{TT} = 0.25$.

Table 2 lists the results of the convergence study through longitudinal and transverse displacements of the middle surface $\overline{u}_1$ and $\overline{u}_3$ at point A choosing three SaS inside each layer for the angle-ply plate strips with stacking sequences [−45/45/−45/45] and [30/−60/−60/30]. A comparison with the ANSYS Solid45 element is also given. It is seen that only one loading step and six iterations are needed to find the converged solution with the chosen criterion and tolerance. The use of coarse meshes is also available. Table 3 exhibits the monotonic convergence of the Newton-Raphson method via the Euclidean norm of displacement and residual vectors during equilibrium iterations for the angle-ply plate strip [−45/45/−45/45] using 32 × 8 mesh when the total load $F = 5$ is applied in one single step.

Figure 5 shows the displacements of the middle surface at point A of laminated plate strips versus tip load F using three SaS for each layer compared to those obtained by ISO7PH element.[20] As can be seen, the results agree closely but the

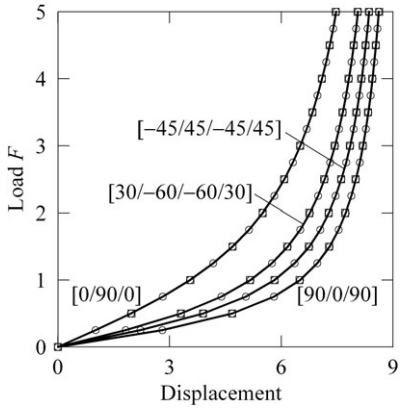

FIGURE 5 Transverse displacement of the middle surface $\overline{u}_3$ (A) of cross-ply and angle-ply plate strips vs tip load F: GeXSaS4 element using three SaS inside each layer and 32 × 8 mesh (○) and ISO7PH element[20] (□)

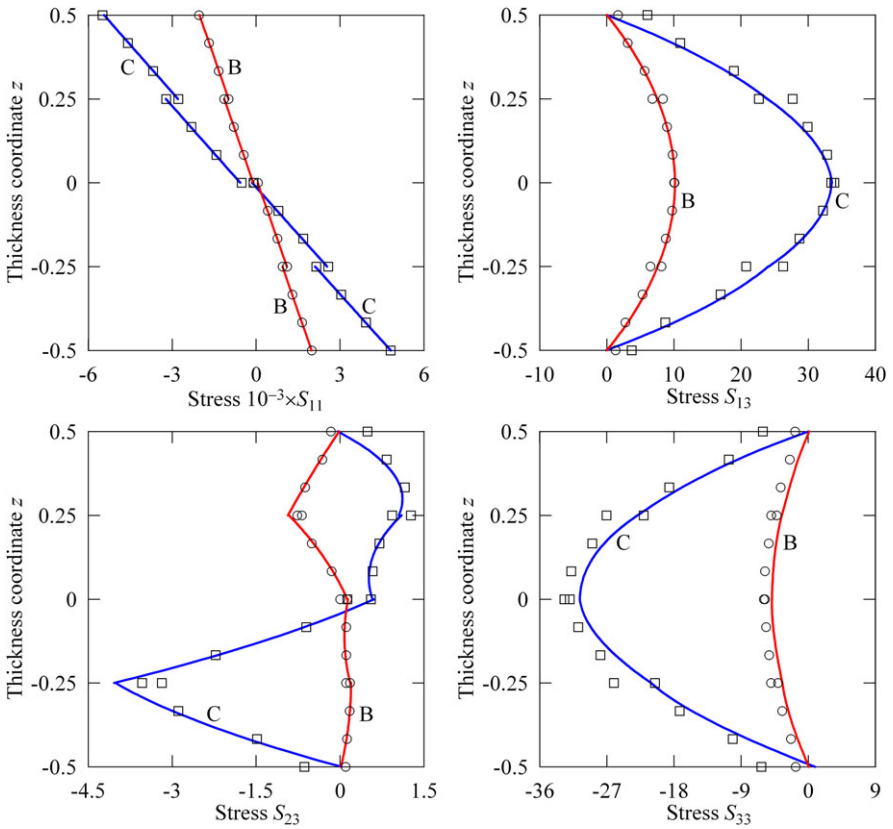

FIGURE 6 Through-thickness distributions of the second Piola-Kirchhoff stress for the angle-ply [−45/45/−45/45] plate strip under tip load $F = 5$ at points B and C: GeXSaS4 element using four SaS inside each layer and 128 × 16 mesh (solid lines) and Solid45 element[60] using 128 × 16 × 3 mesh for each layer (○) and (□) [Colour figure can be viewed at wileyonlinelibrary.com]

developed GeXSaS4 element is less expensive owing to the economical derivation of its tangent stiffness matrix. Figures 6 and 7 present the through-thickness distribution of the second Piola-Kirchhoff stress tensor for the angle-ply plate strips [−45/45/−45/45] and [30/−60/−60/30] at points B and C utilizing four SaS inside the layers and a fine mesh 128 × 16. The results are compared with the Solid45 element using the same fine mesh with three elements through the layer thicknesses that corresponds to a chosen number of SaS. One can see that the Solid45 element leads to a poor prediction for the transverse stresses. It should be noted that it is impossible to satisfy the boundary conditions on bottom and top surfaces and the continuity conditions at interfaces choosing a more number of elements in the thickness direction.

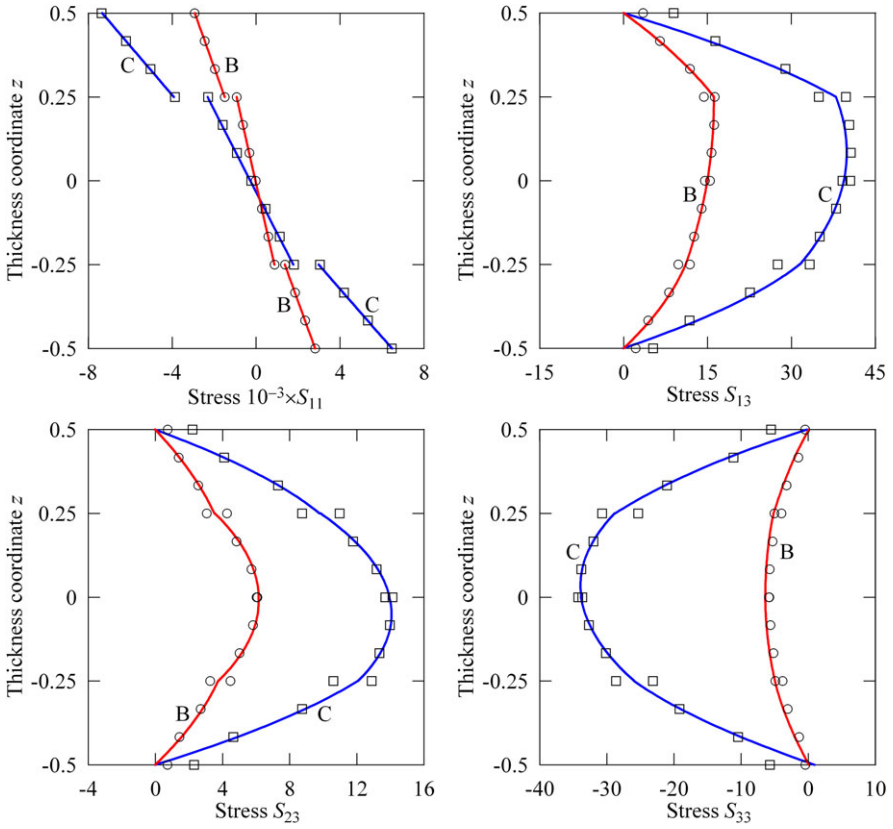

FIGURE 7 Through-thickness distributions of the second Piola-Kirchhoff stress for the angle-ply [30/−60/−60/30] plate strip under load $F = 5$ at points B and C: GeXSaS4 element using four SaS inside each layer and 128×16 mesh (solid lines) and Solid45 element[60] using $128 \times 16 \times 3$ mesh for each layer (○) and (□) [Colour figure can be viewed at wileyonlinelibrary.com]

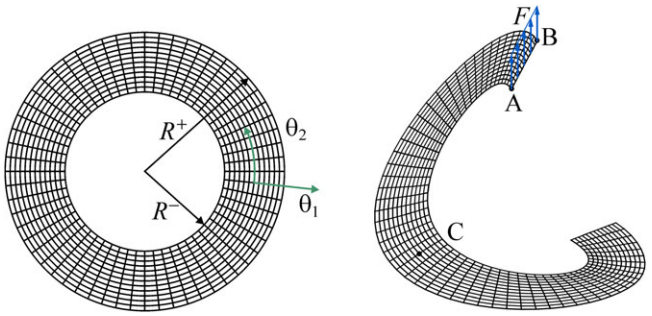

FIGURE 8 Slit annular plate: geometry and deformed configuration of the [90/0/90] plate under load $F = 1.8$ (modeled by 12×60 mesh)

8.2 | Slit annular plate under line load

The annular plate is subjected to a line load F applied at the free edge of the slit as shown in Figure 8, whereas the other edge is fully clamped. Such problem is a good test to verify the ability of the GeXSaS4 element to model rigid-body motions and assess the analytical integration schemes developed. It is apparent that, in the framework of the GeX solid-shell element formulation, we simulate the annular plate as a shell of revolution with the following coefficients of the first and second fundamental forms and Christoffel symbols:

$$\begin{aligned} &A_1 = 1, \quad A_2 = \theta_1, \quad k_1 = 0, \quad k_2 = 0, \\ &B_1 = 0, \quad B_2 = 1/\theta_1, \quad \theta_1 \in \left[R^-, R^+\right], \quad \theta_2 \in [0, 2\pi]. \end{aligned} \tag{87}$$

We consider laminated composite plates with the material properties $E_L = 2 \times 10^7$, $E_T = 6 \times 10^6$, $G_{LT} = 3 \times 10^6$, $G_{TT} = 2.4 \times 10^6$, $\nu_{LT} = 0.3$, and $\nu_{TT} = 0.25$. The geometric parameters are taken to be $R^- = 6$, $R^+ = 10$, and $h = 0.03$. Table 4

TABLE 4 Convergence study for the [90/0/90] annular plate under lifting load $F = 1.8$ using the displacement-based criterion with $\varepsilon = 10^{-4}$

	$I_1 = I_2 = I_3 = 3$						$I_1 = I_2 = I_3 = 4$					
Mesh	**2 × 10**	**4 × 20**	**6 × 30**	**8 × 40**	**12 × 60**	**24 × 120**	**2 × 10**	**4 × 20**	**6 × 30**	**8 × 40**	**12 × 60**	**24 × 120**
$\overline{u}_3$ (A)	13.91	13.91	14.30	14.49	14.64	14.75	13.94	13.91	14.31	14.49	14.65	14.75
$\overline{u}_3$ (B)	17.22	17.31	17.72	17.92	18.07	18.18	17.25	17.32	17.72	17.92	18.07	18.17
NStep	2	3	3	3	3	5	3	3	3	3	3	5
NIter	14	14	16	15	21	23	15	14	16	15	21	23

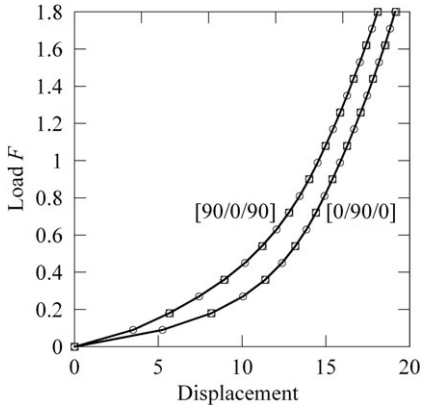

FIGURE 9 Transverse displacements of the middle surface $\overline{u}_3$ (B) of cross-ply annular plates vs load F: GeXSaS4 element using three SaS inside each layer and 12 × 60 mesh (○) and GeX7PH element[17] (□)

presents the results of the convergence study due to mesh refinement for the cross-ply plate [90/0/90] subjected to load $F = 1.8$ via transverse displacements of the middle surface at points A and B using three and four SaS inside the layers. To obtain a converged solution with the chosen criterion and tolerance, we utilized for different finite element meshes from two to five equal load steps.

Figure 9 displays the load-displacement curves for cross-ply composite annular plates using three SaS inside each layer and 12 × 60 mesh. A comparison with the GeX7PH element[17] is also given. Figure 10 shows the through-thickness distribution of the second Piola-Kirchhoff stress tensor at point C$(8, \pi)$ for the composite plate [90/0/90] with three and four SaS for each layer. These results demonstrate the high potential of the GeXSaS4 element because the boundary conditions on bottom and top surfaces and the continuity conditions at interfaces for transverse stress components are satisfied well in the case of using more than three SaS inside the layers.

8.3 | Cylindrical shell with free edges under pulling forces

Next, we consider one of the most popular benchmarks.[8,14,17,20,61] A cylindrical shell with free edges is subjected to opposite pulling forces F. This example is a severe test for nonlinear finite elements because the shell undergoes very large displacements and rotations (see Figure 11). We study an isotropic shell with the material properties $E = 1.05 \times 10^7$ and $\nu = 0.3125$, and cross-ply composite shells with the material properties $E_{\mathrm{L}} = 10^7$, $E_{\mathrm{T}} = 0.3 \times 10^7$, $G_{\mathrm{LT}} = 0.15 \times 10^7$, $G_{\mathrm{TT}} = 0.12 \times 10^7$, and $\nu_{\mathrm{LT}} = \nu_{\mathrm{TT}} = 0.25$. The geometric parameters of cylindrical shells are $L = 10.35$, $R = 4.953$, and $h = 0.094$.

Due to symmetry of the problem, only one octant of the shell is modeled by regular meshes depicted in Figure 11. Table 5 lists the results of the convergence study through the transverse displacements of the middle surface at points A, B, and C using three SaS inside each layer for the cross-ply cylindrical shells with stacking sequences [0/90] and [90/0] under pulling forces $F = 6000$ compared to the ANSYS Solid45 element. The stacking sequence [0/90] implies that the fibers coincide with the axial and circumferential directions in inner and outer layers, respectively. It is seen that, again, only one load step with from 7 to 11 Newton iterations is needed to find the converged solution with the chosen criterion and tolerance except for the [90/0] shell with a fine mesh. Table 6 shows the time taken by a PC (AMD Ryzen 7 2700X CPU 8-Core Processor, 4.0 GHz) to execute one Newton iteration for equivalent single-layer models[18,23] using the GeX7P4 and GeX9P4 elements and the developed layerwise model with a different number of SaS using the GeXSaS4 element.

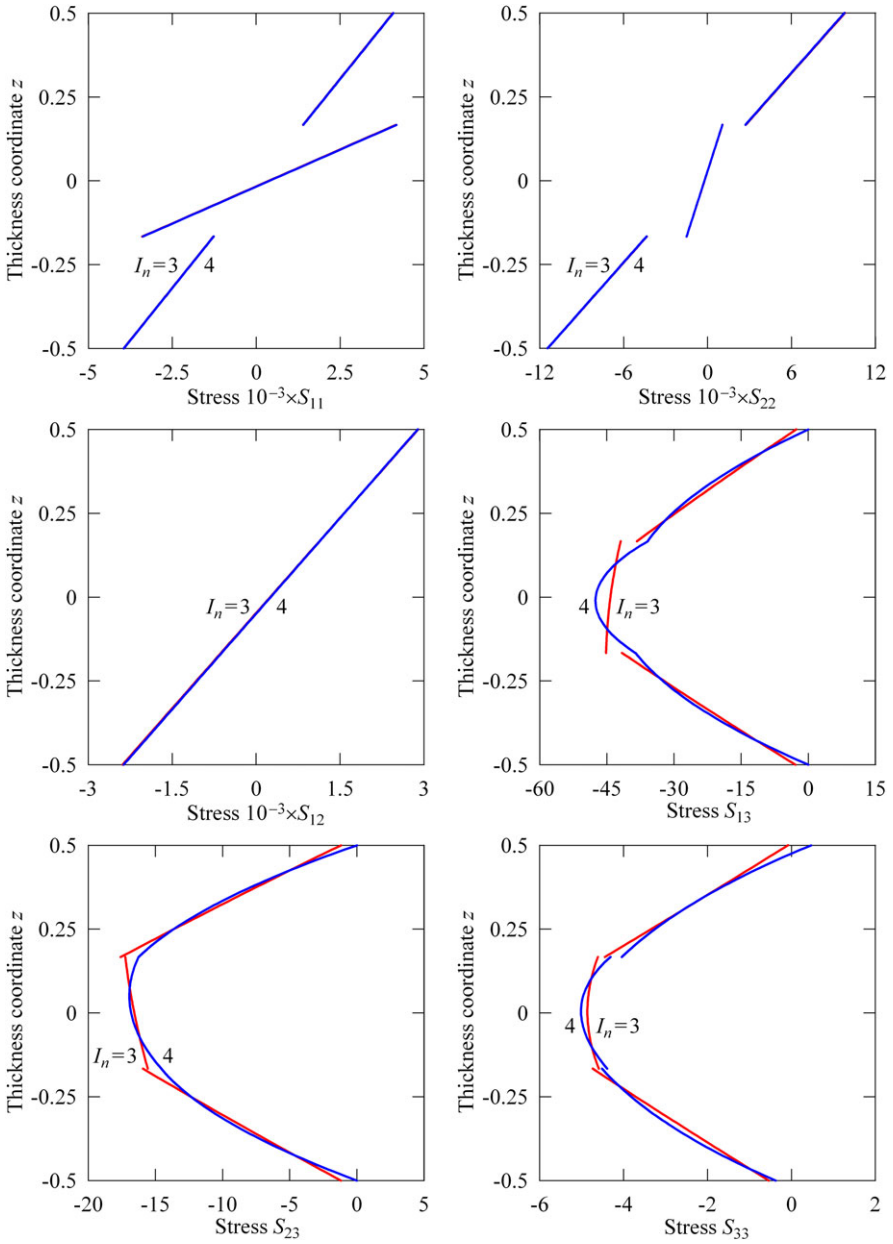

FIGURE 10 Through-thickness distribution of the second Piola-Kirchhoff stress for the cross-ply [90/0/90] annular plate under load $F = 1.8$ at point C for a different number of SaS inside each layer I_n ($n = 1, 2$, and 3) using 24×120 mesh [Colour figure can be viewed at wileyonlinelibrary.com]

The rows of Table 6 display the computation time needed for coarse and fine meshes normalized with respect to the time of the seven-parameter model.

Figures 12 and 13 present load-displacement curves for the isotropic and laminated cylindrical shells using three SaS for each layer compared to those obtained by Sze et al.[61] As can be seen, the results agree closely. Figures 14 and 15 show the through-thickness distribution of the second Piola-Kirchhoff stress tensor for composite cylindrical shells [0/90] and [90/0] at point D($L/4, \pi/4$) using three and four SaS inside the layers and 36×54 mesh. The results are compared with the Solid45 element using the same fine mesh with three elements through the layer thicknesses that corresponds to a selected number of SaS. It is seen that the Solid45 element leads again to a poor distribution of the transverse stress components of the second Piola-Kirchhoff stress tensor. Note that this one does not allow the fulfillment of boundary conditions on the bottom and top surfaces and continuity conditions at the interfaces even in the case of using a larger number of elements in the thickness direction.

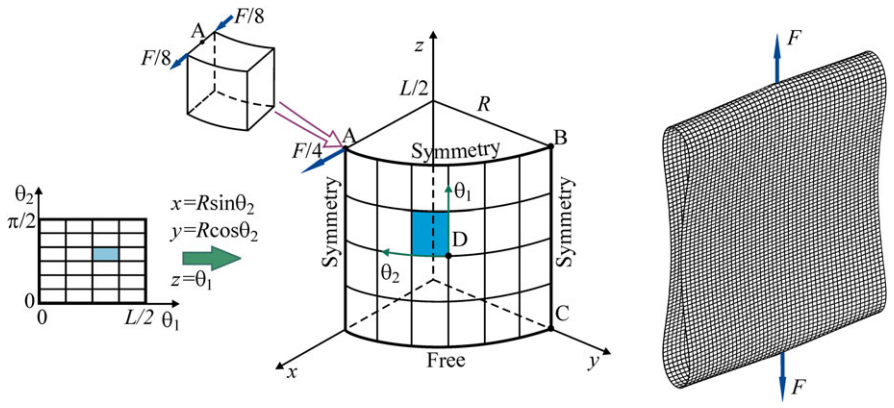

FIGURE 11 One octant of the cylindrical shell under pulling forces: geometry and deformed configuration in the case of the isotropic material and $F = 20\,000$ (modeled by 24×36 mesh)

TABLE 5 Convergence study for the cross-ply cylindrical shells under pulling forces $F = 6000$ using three SaS inside each layer and the displacement-based criterion with $\epsilon = 10^{-4}$

	[0/90]						[90/0]					
Mesh	**4 × 6**	**8 × 12**	**16 × 24**	**24 × 36**	**36 × 54**	**Solid45[a] 36 × 54**	**4 × 6**	**8 × 12**	**16 × 24**	**24 × 36**	**36 × 54**	**Solid45[a] 36 × 54**
$\overline{u}_3$ (A)	2.165	2.269	2.309	2.319	2.326	2.311	2.117	2.229	2.268	2.279	2.284	2.291
$-\overline{u}_3$ (B)	3.584	3.303	3.342	3.350	3.353	3.334	3.429	3.254	3.294	3.302	3.305	3.314
$-\overline{u}_3$ (C)	3.157	3.412	3.446	3.452	3.456	3.433	3.181	3.396	3.429	3.436	3.438	3.447
NStep	1	1	1	1	1	13	1	1	1	1	4	11
NIter	9	7	7	7	11	76	7	7	7	7	29	72

[a]Two elements were used through the layer thickness that corresponds to a chosen number of SaS.

TABLE 6 CPU time required to execute one Newton iteration

Mesh	**Equivalent Single-Layer Models**		**Layerwise Model (GeXSaS4 Element)**		
	7-Parameter Model (GeX7P4 Element)	**9-Parameter Model (GeX9P4 Element)**	$I_1 = I_2 = 3$	$I_1 = I_2 = 4$	$I_1 = I_2 = 5$
4 × 6	1	2.9	35	94	244
16 × 24	1	2.6	26	76	178
36 × 54	1	2.3	22	63	133

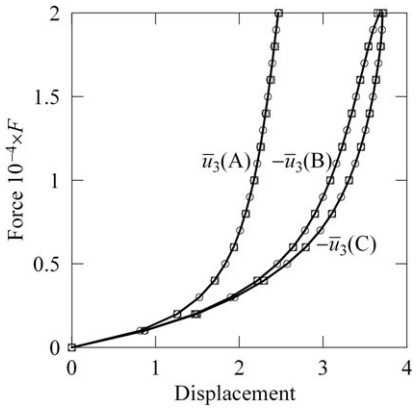

FIGURE 12 Transverse displacements of the middle surface at points A, B, and C of the isotropic cylindrical shell vs force F: GeXSaS4 element using three SaS and 24×36 mesh (○) and ABAQUS S4R element[61] (□)

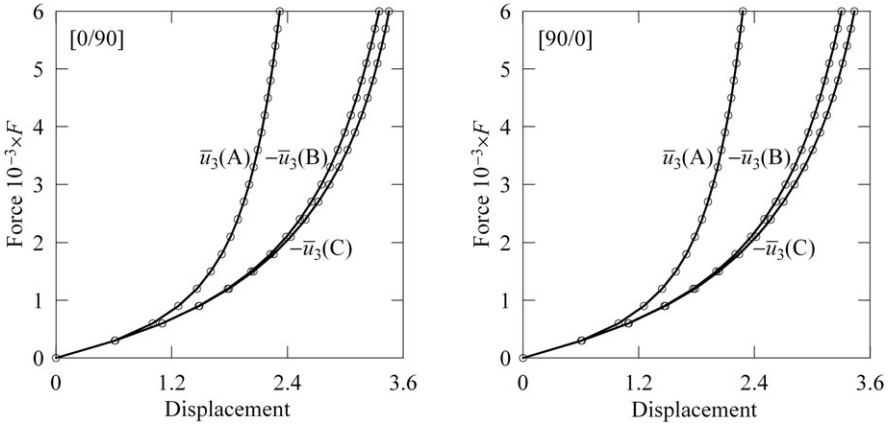

FIGURE 13 Transverse displacements of the middle surface at points A, B, and C of the cross-ply cylindrical shells vs force F: GeXSaS4 element using three SaS inside each layer and 24×36 mesh (○)

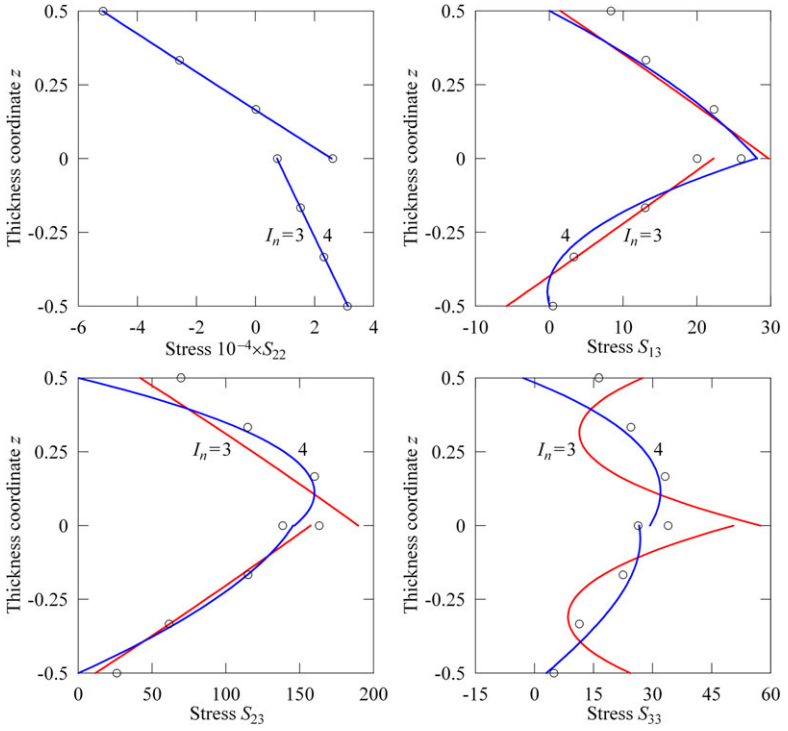

FIGURE 14 Through-thickness distribution of the second Piola-Kirchhoff stress for the [90/0] cylindrical shell under force $F = 6000$ at point D: GeXSaS4 element for a different number of SaS inside each layer I_n ($n = 1$ and 2) using 36×54 mesh (solid lines) and Solid45 element using $36 \times 54 \times 3$ mesh for each layer (○) [Colour figure can be viewed at wileyonlinelibrary.com]

8.4 | Cross-ply hyperbolic shell under two pairs of pulling and pinching forces

Finally, we study laminated composite hyperbolic shells with the stacking sequences [90/0/90] and [0/90/0] under two pairs of opposite pulling and pinching forces $F = 400$. This problem is an excellent benchmark to test additionally the proposed analytical integration schemes because we deal here with a doubly curved shell with variable coefficients of the first and second fundamental forms and Christoffel symbols of the middle surface (parameters ρ and τ are given in Figure 16):

$$A_1 = \sqrt{1 + \frac{\tau^2\theta_1^2}{\rho^2}}, \quad A_2 = \rho, \quad k_1 = -\frac{\tau r^2}{\rho^3 A_1^3}, \quad k_2 = \frac{1}{\rho A_1},$$
$$B_1 = 0, \quad B_2 = \frac{\tau\theta_1}{\rho^2 A_1}, \quad \theta_1 \in [-L, L], \quad \theta_2 \in [0, 2\pi]. \tag{88}$$

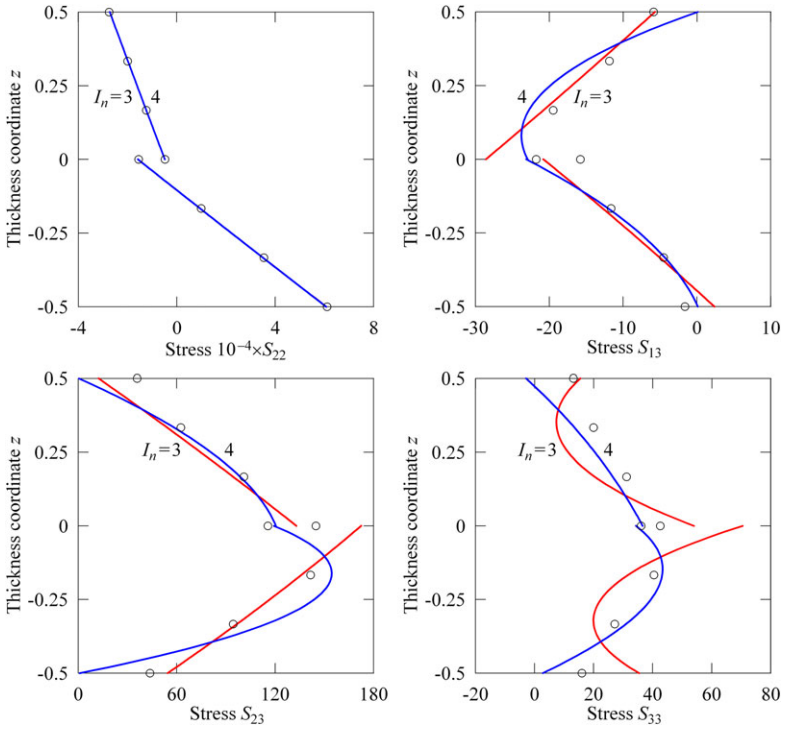

FIGURE 15 Through-thickness distribution of the second Piola-Kirchhoff stress for the [0/90] cylindrical shell under force $F = 6000$ at point D: GeXSaS4 element for a different number of SaS inside each layer I_n ($n = 1$ and 2) using 36×54 mesh (solid lines) and Solid45 element using $36 \times 54 \times 3$ mesh for each layer (○) [Colour figure can be viewed at wileyonlinelibrary.com]

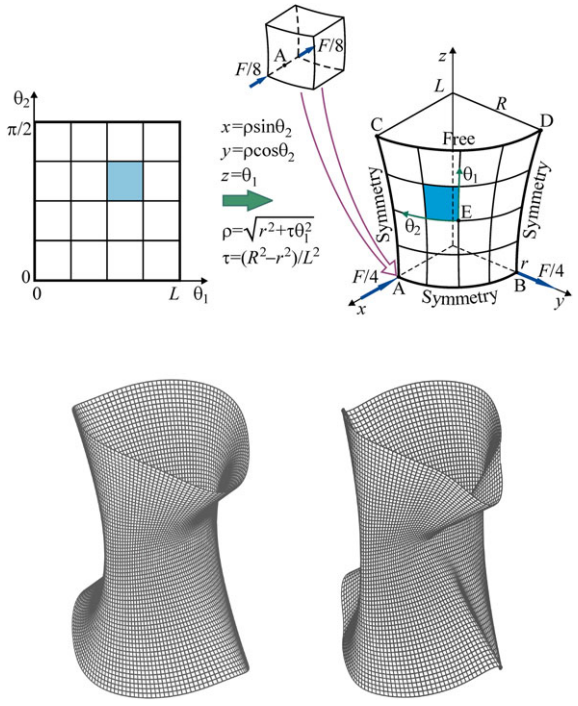

FIGURE 16 One octant of the cross-ply hyperbolic shell under two pairs of pulling and pinching forces: geometry and deformed configurations for [90/0/90] shell (left figure) and [0/90/0] shell (right figure); modeled by using three SaS inside each layer and 32×32 mesh

The geometric parameters of the shell are $L = 20$, $r = 7.5$, $R = 15$, and $h = 0.04$. The material properties of the composite are taken as $E_L = 4 \times 10^7$, $E_T = 10^6$, $G_{LT} = G_{TT} = 6 \times 10^5$, and $\nu_{LT} = \nu_{TT} = 0.25$. Due to symmetry of the problem, only one octant of the shell is modeled by regular meshes depicted in Figure 16. Table 7 lists the results of the convergence study due to mesh refinement via the transverse displacements of the middle surface at points A and C choosing three SaS inside the layers. A comparison with the GeX9P4 solid-shell element is presented. Table 8 demonstrates the monotonic convergence of the Newton-Raphson method via the Euclidean norm of displacement and residual vectors during equilibrium iterations for the [90/0/90] shell when the total load $F = 400$ is applied in one single step.

TABLE 7 Convergence study for the cross-ply hyperbolic shells under two pairs of pulling and pinching forces $F = 400$ using three SaS inside each layer and the displacement-based criterion with $\varepsilon = 10^{-4}$

	[90/0/90]						[0/90/0]					
Mesh	**4 × 4**	**8 × 8**	**16 × 16**	**32 × 32**	**48 × 48**	**GeX9P4 32 × 32**	**4 × 4**	**8 × 8**	**16 × 16**	**32 × 32**	**48 × 48**	**GeX9P4 32 × 32**
$-\overline{u}_x$ (A)	2.609	3.159	3.483	3.525	3.536	3.523	3.120	4.773	5.644	6.157	6.198	6.133
$\overline{u}_x$ (C)	2.257	2.438	2.527	2.520	2.519	2.519	2.538	2.916	2.896	2.681	2.659	2.692
NStep	1	2	1	1	1	1	1	2	2	5	6	5
NIter	9	15	8	7	7	7	10	15	19	26	26	26

TABLE 8 Euclidean norm of displacement and residual vectors during equilibrium iterations for the [90/0/90] hyperbolic shell using 32 × 32 mesh when the total load $F = 400$ is applied in one single step

	$\|\| \mathbf{U}^{[n+1]} - \mathbf{U}^{[n]} \|\|$		$\|\| \mathbf{r}^{[n]} \|\|$	
Iteration	$I_1 = I_2 = I_3 = 3$	$I_1 = I_2 = I_3 = 4$	$I_1 = I_2 = I_3 = 3$	$I_1 = I_2 = I_3 = 4$
0	5.18E+02	6.19E+02	1.00E+02	1.00E+02
1	2.57E+02	3.07E+02	2.42E+07	2.43E+07
2	1.15E+02	1.37E+02	4.34E+06	4.36E+06
3	4.10E+01	4.90E+01	8.20E+05	8.24E+05
4	1.08E+01	1.30E+01	2.01E+05	2.03E+05
5	2.48E+00	2.96E+00	3.96E+04	4.07E+04
6	9.92E−02	1.19E−01	1.91E+03	2.46E+03
7	3.63E−04	4.54E−04	1.58E+01	5.69E+01
8	9.69E−09	7.37E−07	1.02E−03	1.32E+00
9	6.29E−10	1.49E−09	8.52E−08	1.65E−05
10	6.29E−10	1.41E−09	8.55E−08	1.46E−06

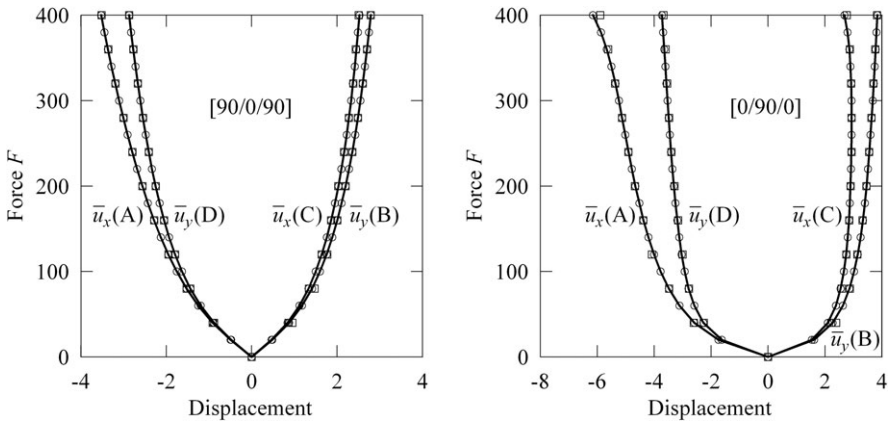

FIGURE 17 Transverse displacements of the middle surface at points A, B, C, and D of the cross-ply cylindrical shells vs force F: GeXSaS4 element using three SaS inside each layer and 32 × 32 mesh (○) and five-parameter shell element of Basar et al.[62] (□)

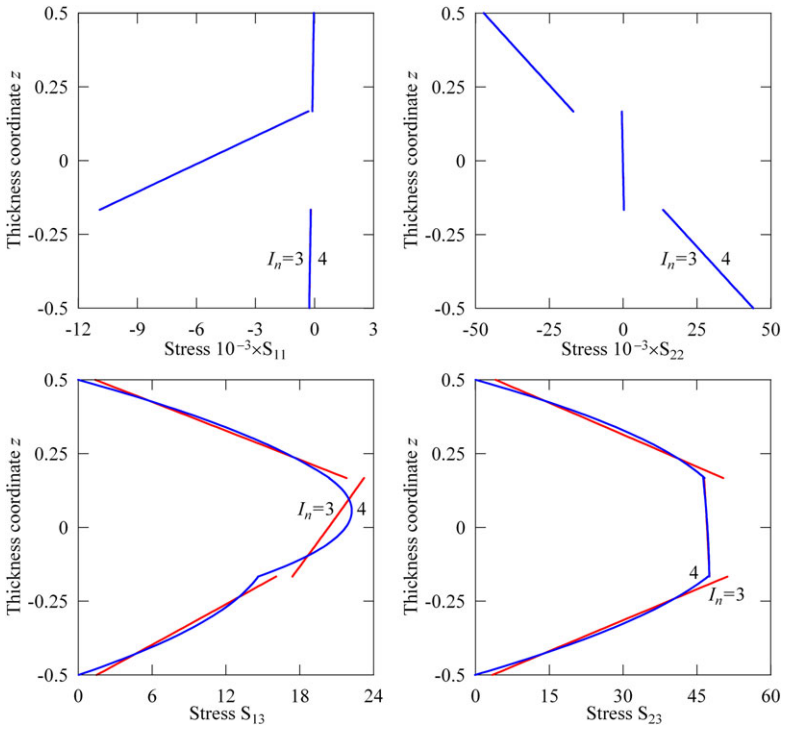

FIGURE 18 Through-thickness distribution of the second Piola-Kirchhoff stress for the cross-ply [90/0/90] hyperbolic shell under force $F = 400$ at point E$(L/2, \pi/4)$ for a different number of SaS inside each layer I_n ($n = 1, 2$, and 3) using 32×32 mesh [Colour figure can be viewed at wileyonlinelibrary.com]

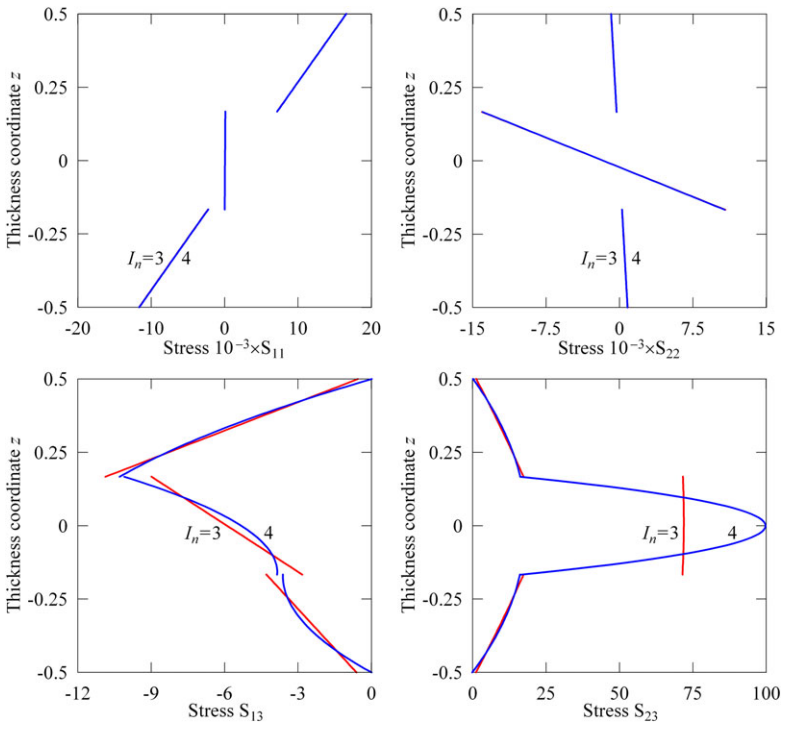

FIGURE 19 Through-thickness distribution of the second Piola-Kirchhoff stress for the cross-ply [0/90/0] hyperbolic shell under force $F = 400$ at point E$(L/2, \pi/4)$ for a different number of SaS inside each layer I_n ($n = 1$,2 and 3) using 32×32 mesh [Colour figure can be viewed at wileyonlinelibrary.com]

Figure 17 shows load-displacement curves related to points A, B, C, and D for both hyperbolic shells using three SaS inside the layers and 32×32 mesh compared to the results in the work of Basar et al.[62] Figures 18 and 19 display the through-thickness distribution of the second Piola-Kirchhoff stress at point E$(L/2, \pi/4)$ taking three and four SaS for each layer. As can be seen, the GeXSaS4 element performs well in the case of using more than three SaS. However, it cannot be employed for the analysis of the transverse normal stress because the shell is very thin with the slenderness ratio $R/h = 375$. There is no such a problem when we analyze thicker hyperbolic shells with $R/h < 250$.

9 | CONCLUSIONS

This paper presents a finite rotation GeX hybrid-mixed four-node solid-shell element based on the SaS method in which the displacements of SaS are utilized as fundamental shell unknowns. The SaS are located at Chebyshev polynomial nodes inside the layers and interfaces as well. The tangent stiffness matrix is evaluated through 3D analytical integration based on the extended ANS method with no expensive numerical matrix inversion and its explicit form is presented. The developed GeXSaS4 solid-shell element passes 3D membrane and bending patch tests[48] and zero energy mode tests[50] and exhibits a superior performance in all benchmarks considered.

The proposed GeX four-node SaS solid-shell element formulation is free of assumptions of small displacements, small rotations and small loading steps. This formulation allows one to employ much larger load increments than possible with existing displacement-based solid-shell elements. Due to this novelty and 3D analytical integration, the GeXSaS4 element allows the use of very coarse meshes even for laminated composite shells undergoing arbitrarily large displacements and rotations. It can be recommended for the analysis of the second Piola-Kirchhoff stress in nonlinear thick and thin composite shells.

The GeXSaS4 solid-shell element can be extended to the analysis of finite rotation functionally graded shell structures following contributions.[17,20,49,50]

ACKNOWLEDGEMENTS

This work was supported by the Russian Science Foundation (grant 18-19-00092) and by the Russian Ministry of Education and Science (grant 9.4914.2017/6.7). The authors wish to thank A.O. Glebov for his assistance with the finite element evaluation.

ORCID

Gennady M. Kulikov https://orcid.org/0000-0002-8243-3461

REFERENCES

1. Kim YH, Lee SW. A solid element formulation for large deflection analysis of composite shell structures. *Comp Struct*. 1988;30:269-274.
2. Yeom CH, Lee SW. An assumed strain finite element model for large deflection composite shells. *Int J Numer Meth Eng*. 1989;28:1749-1768.
3. Braun M, Bischoff M, Ramm E. Non-linear shell formulations for complete three-dimensional constitutive laws including composites and laminates. *Computational Mechanics*. 1994;15:1-18.
4. Sze KY, Chan WK, Pian THH. An eight-node hybrid-stress solid-shell element for geometric non-linear analysis of elastic shells. *Int J Numer Meth Eng*. 2002;55:853-878.
5. Sze KY, Zheng S-J. A stabilized hybrid-stress solid element for geometrically nonlinear homogeneous and laminated shell analyses. *Comput Methods Appl Mech Eng*. 2002;191:1945-1966.
6. Kulikov GM, Plotnikova SV. Non-linear strain–displacement equations exactly representing large rigid-body motions. Part I. Timoshenko–Mindlin shell theory. *Comput Methods Appl Mech Eng*. 2003;192:851-875.
7. Vu-Quok L, Tan XG. Optimal solid shells for non-linear analyses of multilayer composites. I. Statics. *Comput Methods Appl Mech Eng*. 2003;192:975-1016.
8. Kulikov GM, Plotnikova SV. Non-linear strain–displacement equations exactly representing large rigid-body motions. Part II. Enhanced finite element technique. *Comput Methods Appl Mech Eng*. 2006;195:2209-2230.
9. Klinkel S, Gruttmann F, Wagner W. A robust non-linear solid shell element based on a mixed variational formulation. *Methods Appl Mech Eng*. 2006;195:179-201.
10. Parisch H. A continuum-based shell theory for non-linear applications. *Int J Numer Methods Eng*. 1995;38:1855-1883.
11. Sansour C. A theory and finite element formulation of shells at finite deformations involving thickness change: circumventing the use of a rotation tensor. *Arch Appl Mech*. 1995;65:194-216.

12. Basar Y, Itskov M, Eckstein A. Composite laminates: nonlinear interlaminar stress analysis by multi-layer shell elements. *Comput Methods Appl Mech Eng*. 2000;185:367-397.
13. El-Abbasi N, Meguid SA. A new shell element accounting for through-thickness deformation. *Comput Methods Appl Mech Eng*. 2000;189:841-862.
14. Sansour C, Kollmann FG. Families of 4-node and 9-node finite elements for a finite deformation shell theory. An assessment of hybrid stress, hybrid strain and enhanced strain elements. *Computational Mechanics*. 2000;24:435-447.
15. Brank B, Korelc J, Ibrahimbegović A. Nonlinear shell problem formulation accounting for through-the-thickness stretching and its finite element implementation. *Comput Struct*. 2002;80:699-717.
16. Brank B. Nonlinear shell models with seven kinematic parameters. *Comput Methods Appl Mech Eng*. 2005;194:2336-2362.
17. Arciniega RA, Reddy JN. Tensor-based finite element formulation for geometrically nonlinear analysis of shell structures. *Comput Methods Appl Mech Eng*. 2007;196:1048-1073.
18. Kulikov GM, Plotnikova SV. Finite rotation geometrically exact four-node solid-shell element with seven displacement degrees of freedom. *Comput Model Eng Sciences*. 2008;28:15-38.
19. Kulikov GM, Plotnikova SV. Calculation of composite structures subjected to follower loads by using a geometrically exact shell element. *Mech Compos Mater*. 2009;45:545-556.
20. Payette GS, Reddy JN. A seven-parameter spectral/*hp* finite element formulation for isotropic, laminated composite and functionally graded shell structures. *Comput Methods Appl Mech Eng*. 2014;278:664-704.
21. Frikha A, Dammak F. Geometrically non-linear static analysis of functionally graded material shells with a discrete double directors shell element. *Comput Methods Appl Mech Eng*. 2017;315:1-24.
22. Hajlaoui A, Triki E, Frikha A, Wali M, Dammak F. Nonlinear dynamics analysis of FGM shell structures with a higher order shear strain enhanced solid-shell element. *Latin Amer J Solids Struct*. 2017;14:72-91.
23. Kulikov GM, Plotnikova SV. Non-linear exact geometry 12-node solid-shell element with three translational degrees of freedom per node. *Int J Numer Methods Eng*. 2011;88:1363-1389.
24. Kulikov GM, Plotnikova SV. Finite rotation piezoelectric exact geometry solid-shell element with nine degrees of freedom per node. *Comp Mater Continua*. 2011;23:233-264.
25. Roh HY, Cho M. The application of geometrically exact shell elements to B-spline surfaces. *Comput Methods Appl Mech Eng*. 2004;193:2261-2299.
26. Hughes TJR, Cottrell JA, Bazilevs Y. Isogeometric analysis: CAD, finite elements, NURBS, exact geometry and mesh refinement. *Comput Methods Appl Mech Eng*. 2005;194:4135-4195.
27. Cottrell JA, Hughes TJR, Bazilevs Y. *Isogeometric Analysis: Toward Integration of CAD and FEA*. Singapore: Wiley; 2009.
28. Bazilevs Y, Calo VM, Cottrell JA, et al. Isogeometric analysis using T-splines. *Comput Methods Appl Mech Eng*. 2010;199:229-263.
29. Benson DJ, Bazilevs Y, Hsu MC, Hughes TJR. Isogeometric shell analysis: the Reissner–Mindlin shell. *Comput Methods Appl Mech Eng*. 2010;199:276-289.
30. Echter R, Bischoff M. Numerical efficiency, locking and unlocking of NURBS finite elements. *Comput Methods Appl Mech Eng*. 2010;199:374-382.
31. Dörfel MR, Jüttler B, Simeon B. Adaptive isogeometric analysis by local h-refinement with T-splines. *Comput Methods Appl Mech Eng*. 2010;199:264-275.
32. Lipton S, Evans JA, Bazilevs Y, Elguedj T, Hughes TJR. Robustness of isogeometric structural discretizations under severe mesh distortion. *Comput Methods Appl Mech Eng*. 2010;199:357-373.
33. Nguyen-Thanh N, Nguyen-Xuan H, Bordas SPA, Rabczuk T. Isogeometric analysis using polynomial splines over hierarchical T-meshes for two-dimensional elastic solids. *Comput Methods Appl Mech Eng*. 2011;200:1892-1908.
34. Thai CH, Nguyen-Xuan H, Bordas SPA, Nguyen-Thanh N, Rabczuk T. Isogeometric analysis of laminated composite plates using the higher-order shear deformation theory. *Mech Adv Mater Struct*. 2015;22:451-469.
35. Nguyen-Thanh N, Zhou K, Zhuang X, et al. Isogeometric analysis of large-deformation thin shells using RHT-splines for multiple-patch coupling. *Comput Methods Appl Mech Eng*. 2017;316:1157-1178.
36. Vu-Bac N, Duong TX, Lahmer T, et al. A NURBS-based inverse analysis for reconstruction of nonlinear deformations of thin shell structures. *Comput Methods Appl Mech Eng*. 2018;331:427-455.
37. Grigolyuk EI, Kulikov GM. Axisymmetric deformation of anisotropic multilayered shells of revolution of intricate shapes. *Mech Compos Mater*. 1982;17:437-445. https://doi.org/10.1007/BF00605911
38. Grigolyuk EI, Kulikov GM. *Multilayered Reinforced Shells: Analysis of Pneumatic Tires*. Moscow, Russia: Mashinostroyenie; 1988. Russian.
39. Noor AK, Tanner JA, Peters JM. Sensitivity of tire response to variations in material and geometric parameters. *Finite Elem Anal Design*. 1992;11:77-86.
40. Noor AK, Tanner JA, Peters JM. Reduced basis technique for evaluating sensitivity derivatives of the nonlinear response of the space shuttle orbiter nose-gear tire. *Tire Sci Technol*. 1993;21:232-259.
41. Kulikov GM. Computational models for multilayered composite shells with application to tires. *Tire Sci Technol*. 1996;24:11-38.
42. Kulikov GM, Plotnikova SV. Non-linear geometrically exact assumed stress-strain four-node solid-shell element with high coarse-mesh accuracy. *Finite Elem Anal Design*. 2007;43:425-443.
43. Coda HB, Paccola RR, Carrazedo R. Zig-Zag effect without degrees of freedom in linear and non linear analysis of laminated plates and shells. *Compos Struct*. 2017;161:32-50.

44. Carrazedo R, Coda HB. Triangular based prismatic finite element for the analysis of orthotropic laminated beams, plates and shells. *Compos Struct*. 2017;168:234-246.
45. Gruttmann F, Knust G, Wagner W. Theory and numerics of layered shells with variationally embedded interlaminar stresses. *Comput Methods Appl Mech Eng*. 2017;326:713-738.
46. Kulikov GM, Plotnikova SV. On the use of a new concept of sampling surfaces in a shell theory. *Adv Struct Mater*. 2011;15:715-726.
47. Kulikov GM, Plotnikova RS. Solution of three-dimensional problems for thick elastic shells by the method of reference surfaces. *Mech Solids*. 2014;49:403-412.
48. Kulikov GM, Plotnikova SV. A hybrid-mixed four-node quadrilateral plate element based on sampling surfaces method for 3D stress analysis. *Int J Numer Methods Eng*. 2016;108:26-54.
49. Kulikov GM, Plotnikova SV. Exact geometry SaS solid-shell element for 3D stress analysis of FGM piezoelectric structures. *Curved Layered Struct*. 2018;5:116-135.
50. Kulikov GM, Plotnikova SV. Exact geometry four-node solid-shell element for stress analysis of functionally graded shell structures via advanced SaS formulation. *Mech Adv Mater Struct*. 2019. https://doi.org/10.1080/15376494.2018.1502380
51. Kulikov GM, Plotnikova SV. Analysis of the second Piola-Kirchhoff stress in non-linear thick and thin structures using exact geometry SaS solid-shell elements. *Int J Numer Methods Eng*. 2019;117:498-522.
52. Pian THH. State-of-the-art development of hybrid/mixed finite element method. *Finite Elem Anal Design*. 1995;21:5-20.
53. Pian THH, Sumihara K. Rational approach for assumed stress finite elements. *Int J Numer Methods Eng*. 1984;20:1685-1695.
54. Lee SW, Pian THH. Improvement of plate and shell finite elements by mixed formulations. *AIAA J*. 1978;16:29-34.
55. Wempner G, Talaslidis D, Hwang C-M. A simple and efficient approximation of shells via finite quadrilateral elements. *J Appl Mech*. 1982;49:115-120.
56. Betsch P, Stein E. An assumed strain approach avoiding artificial thickness straining for a nonlinear 4-node shell element. *Commun Numer Methods Eng*. 1995;11:899-909.
57. Atluri S. On the hybrid stress finite element model for incremental analysis of large deflection problems. *Int J Solids Struct*. 1973;9:1177-1191.
58. Boland PL, Pian THH. Large deflection analysis of thin elastic structures by the assumed stress hybrid finite element method. *Comp Struct*. 1977;7:1-12.
59. Cho C, Lee SW. On the assumed strain formulation for geometrically nonlinear analysis. *Finite Elem Anal Design*. 1996;24:31-47.
60. ANSYS: Version 5.6. Canonsburg, PA: ANSYS Inc; 1999.
61. Sze KY, Liu XH, Lo SH. Popular benchmark problems for geometric nonlinear analysis of shells. *Finite Elem Anal Design*. 2004;40:1551-1569.
62. Basar Y, Ding Y, Schultz R. Refined shear-deformation models for composite laminates with finite rotations. *Int J Solids Struct*. 1993;30:2611-2638.

How to cite this article: Kulikov GM, Plotnikova SV. Finite rotation exact geometry solid-shell element for laminated composite structures through extended SaS formulation and 3D analytical integration. *Int J Numer Methods Eng*. 2019;119:852–878. https://doi.org/10.1002/nme.6075

APPENDIX A

The nodal vectors $\Xi_{ijr}^{(n)i_n}$ introduced in Section 6 to define the strain parameters and displacement derivatives of SaS at element nodes (48) can be written in a closed form. The use of Equations (17), (22), (42), (43), and (47) leads to the following expressions for nonzero components of these vectors:

$$
\begin{aligned}
&\left(\Xi_{\alpha\beta r}^{(n)i_n}\right)_{\alpha+3\mu_n+3N_{\mathrm{SaS}}(s-1)} = d_{\beta rs}, \quad \left(\Xi_{\alpha\alpha r}^{(n)i_n}\right)_{3+3\mu_n+3N_{\mathrm{SaS}}(s-1)} = \delta_{rs}k_{\alpha s},\\
&\left(\Xi_{\alpha\alpha r}^{(n)i_n}\right)_{\beta+3\mu_n+3N_{\mathrm{SaS}}(s-1)} = \delta_{rs}B_{\alpha s}, \quad \left(\Xi_{\alpha\beta r}^{(n)i_n}\right)_{\beta+3\mu_n+3N_{\mathrm{SaS}}(s-1)} = -\delta_{rs}B_{\beta s} \text{ for } \beta \neq \alpha,\\
&\left(\Xi_{3\alpha r}^{(n)i_n}\right)_{3+3\mu_n+3N_{\mathrm{SaS}}(s-1)} = d_{\alpha rs}, \quad \left(\Xi_{3\alpha r}^{(n)i_n}\right)_{\alpha+3\mu_n+3N_{\mathrm{SaS}}(s-1)} = -\delta_{rs}k_{\alpha s},\\
&\left(\Xi_{i3r}^{(n)i_n}\right)_{i+3\nu_n+3N_{\mathrm{SaS}}(s-1)} = \delta_{rs}M^{(n)j_n}\left(\theta_3^{(n)i_n}\right),
\end{aligned}
\tag{A1}
$$

where

$$d_{\alpha rs} = \frac{1}{4\ell_\alpha A_{\alpha r}} n_{\alpha s}\left(1 + n_{\beta r} n_{\beta s}\right) \quad \text{for } \beta \neq \alpha,$$
$$\mu_n = i_n + \sum_{\tau=1}^{n-1} I_\tau - n, \quad \nu_n = j_n + \sum_{\tau=1}^{n-1} I_\tau - n, \tag{A2}$$

where $A_{\alpha r}$, $k_{\alpha r}$, and $B_{\alpha r}$ are the nodal values of geometric parameters of the middle surface; δ_{rs} is the Kronecker delta. The coefficients $n_{\alpha r}$ are defined by (43) and, as we remember, the indices $n = 1, 2, \ldots, N$; $i_n, j_n = 1, 2, \ldots, I_n$; $r, s = 1, 2, 3, 4$; $i = 1, 2, 3$ and $\alpha, \beta = 1, 2$. The remaining components of vectors $\Xi_{ijr}^{(n)i_n}$ not written out explicitly are zero.

APPENDIX B

Here, we formulate two propositions used in Sections 6 and 7.

Proposition 2. *The determinant of the matrix* $\mathbf{\Lambda}^{(n)} = \left[\Lambda^{(n)i_n j_n}\right]$ *related to the nth layer is not equal to zero.*

Proof. Introduce any vector $\mathbf{v}^{(n)} = \left[v_1 v_2 \cdots v_{I_n}\right]^{\mathrm{T}}$ and consider a quadratic form

$$\begin{aligned}\left(\mathbf{v}^{(n)}\right)^{\mathrm{T}} \mathbf{\Lambda}^{(n)} \mathbf{v}^{(n)} &= \sum_{i_n}\sum_{j_n} \Lambda^{(n)i_n j_n} v_{i_n}^{(n)} v_{j_n}^{(n)} \\ &= \sum_{i_n}\sum_{j_n} v_{i_n}^{(n)} v_{j_n}^{(n)} \int_{\theta_3^{[n-1]}}^{\theta_3^{[n]}} L^{(n)i_n} L^{(n)j_n} c_1 c_2 d\theta_3 = \int_{\theta_3^{[n-1]}}^{\theta_3^{[n]}} \left(g^{(n)}\right)^2 c_1 c_2 d\theta_3,\end{aligned} \tag{B1}$$

where

$$g^{(n)}(\theta_3) = \sum_{i_n} v_{i_n}^{(n)} L^{(n)i_n}. \tag{B2}$$

Because of $c_\alpha > 0$, the quadratic form $(\mathbf{v}^{(n)})^{\mathrm{T}} \mathbf{\Lambda}^{(n)} \mathbf{v}^{(n)}$ is positive definite and, therefore, $\det(\mathbf{\Lambda}^{(n)}) > 0$. □

Proposition 3. *For any vector* $\mathbf{w} = [w_1\ w_2\ w_3\ w_4\ w_5\ w_6]^T$, *the identity*

$$\left(\mathbf{A}_{r_1 r_2}^{(n)i_n}(\mathbf{q})\right)^{\mathrm{T}} \mathbf{w} = \mathbf{H}_{r_1 r_2}^{(n)i_n}(\mathbf{w})\,\mathbf{q} \quad \textit{for} \quad r_1 + r_2 < 2 \tag{B3}$$

holds, where $\mathbf{H}_{r_1 r_2}^{(n)i_n}(\mathbf{w})$ *are the symmetric matrices of order* $12N_{SaS} \times 12N_{SaS}$ *defined as*

$$\mathbf{H}_{r_1 r_2}^{(n)i_n}(\mathbf{w}) = w_1 \mathbf{\Pi}_{11 r_1 r_2}^{(n)i_n} + w_2 \mathbf{\Pi}_{22 r_1 r_2}^{(n)i_n} + w_3 \mathbf{\Pi}_{33 r_1 r_2}^{(n)i_n} + w_4 \mathbf{\Pi}_{12 r_1 r_2}^{(n)i_n} + w_5 \mathbf{\Pi}_{13 r_1 r_2}^{(n)i_n} + w_6 \mathbf{\Pi}_{23 r_1 r_2}^{(n)i_n}. \tag{B4}$$

Proof. The symmetry of matrices $\mathbf{H}_{r_1 r_2}^{(n)i_n}(\mathbf{w})$ follows from the symmetry of matrices $\mathbf{\Pi}_{ijr_1 r_2}^{(n)i_n}$ given by Equations (51) and (57). Owing to this property and Equation (56), we have

$$\left(\mathbf{A}_{r_1 r_2}^{(n)i_n}(\mathbf{q})\right)^{\mathrm{T}} \mathbf{w} = \left[\mathbf{\Pi}_{11 r_1 r_2}^{(n)i_n}\mathbf{q}\ \mathbf{\Pi}_{22 r_1 r_2}^{(n)i_n}\mathbf{q}\ \mathbf{\Pi}_{33 r_1 r_2}^{(n)i_n}\mathbf{q}\ \mathbf{\Pi}_{12 r_1 r_2}^{(n)i_n}\mathbf{q}\ \mathbf{\Pi}_{13 r_1 r_2}^{(n)i_n}\mathbf{q}\ \mathbf{\Pi}_{23 r_1 r_2}^{(n)i_n}\mathbf{q}\right] \mathbf{w} = \mathbf{H}_{r_1 r_2}^{(n)i_n}(\mathbf{w})\,\mathbf{q} \tag{B5}$$

that completes the proof. □